

CT-OT Flow: Estimating Continuous-Time Dynamics from Discrete Temporal Snapshots

Keisuke Kawano*, Takuro Kutsuna, Naoki Hayashi, Yasushi Esaki, Hidenori Tanaka

Toyota Central R&D Labs., Inc., Japan

*kawano@mosk.tytlabs.co.jp

Abstract

In many real-world scenarios, such as single-cell RNA sequencing, data are observed only as discrete-time snapshots spanning finite time intervals and subject to noisy timestamps, with no continuous trajectories available. Recovering the underlying continuous-time dynamics from these snapshots with coarse and noisy observation times is a critical and challenging task. We propose Continuous-Time Optimal Transport Flow (CT-OT Flow), which first infers high-resolution time labels via partial optimal transport and then reconstructs a continuous-time data distribution through a temporal kernel smoothing. This reconstruction enables accurate training of dynamics models such as ODEs and SDEs. CT-OT Flow consistently outperforms state-of-the-art methods on synthetic benchmarks and achieves lower reconstruction errors on real scRNA-seq and typhoon-track datasets. Our results highlight the benefits of explicitly modeling temporal discretization and timestamp uncertainty, offering an accurate and general framework for bridging discrete snapshots and continuous-time processes.

1 Introduction

In various fields such as biology [1, 2], urban studies [3], and medical data analysis [4], data are often collected not continuously but as *discrete temporal snapshots*, i.e., at distinct points in time. Researchers then need to estimate the underlying dynamics of individual data points from these snapshots. For example, in single-cell RNA sequencing (scRNA-seq) [5], cellular dynamics are inferred from discrete temporal snapshots at different culture durations because cells are destroyed during measurement, making it impossible to track each cell over time. Similarly, in urban mobility studies [6] or environmental sensor data [7], it is challenging to continuously track individuals or sensors, and one typically only obtains data sampled at coarse time intervals. Estimating the trajectories (or dynamics) of individual data points from these temporal snapshots is a critically important task for both scientific discovery and practical applications.

To model such dynamics, continuous normalizing flow [8] and Schrödinger bridge [9]-based methods [1, 2, 10] have been proposed. These methods fit ordinary differential equations (ODEs) or stochastic differential equations (SDEs) to temporal snapshots, and thereby infer time-evolving trajectories. However, they face two major limitations: **(1) Time discretization.** Due to constraints such as measurement costs and data sparsity, temporal snapshots are often recorded at discrete intervals. Consequently, all data points collected within the same interval are forced to share a single, coarse-grained time label. For instance, in scRNA-seq experiments [11], cells harvested between day 1 and day 3 may be labeled as $t = 1$, and those harvested between day 4 and day 6 as $t = 2$. Methods that ignore this discretization may naively assume that all $t = 1$ cells transition directly to $t = 2$ along the shortest path in feature space, yielding suboptimal or even misleading dynamics. **(2) Time-label uncertainty.** The recorded times themselves can be noisy. In scRNA-seq experiments, individual cells’ true “birth times” cannot be directly measured, introducing uncertainty into the

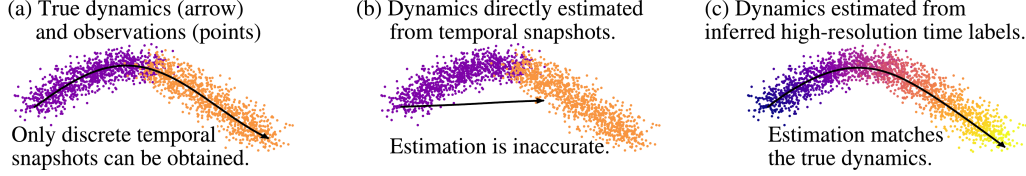


Figure 1: Motivating example for CT-OT Flow. (a) True dynamics (arrow) and observations (points). (b) Dynamics estimated directly from the discrete timestamps are inaccurate. (c) CT-OT Flow: Dynamics recovered accurately follow the ground truth by inferring high-resolution time labels.

observation timestamps [12]. Ignoring this uncertainty when estimating dynamics can result in a model that diverges from the true process.

In this work, we propose **Continuous-Time Optimal Transport Flow (CT-OT Flow)**, a method designed to address both time discretization and time-label uncertainty in order to recover more accurate dynamics. CT-OT Flow has two major components. **(1) High-resolution time label inference via partial optimal transport.** CT-OT Flow employs partial optimal transport (POT) [13, 14] to infer high-resolution time labels for each data point, even if the raw observations are aggregated into discrete intervals. By leveraging POT, we can incorporate sample similarities when estimating high-resolution time labels. **(2) Kernel-based construction of data distribution in continuous-time.** CT-OT Flow then builds data distributions in continuous-time via a kernel-based smoothing approach. This step enables robust estimation of ODE/SDE even in the presence of substantial noise or uncertainty in the times. Unlike existing methods [2, 10] that simply ignore potential misalignment in time labels, CT-OT Flow can approximate real-world dynamics more accurately.

Figure 1(a) illustrates a toy 2-D example, where the arrow represents the true dynamics and points indicate observations with discrete timestamps, shown in purple and orange. Even though the true dynamics follow a curved path (Fig. 1(a)), estimating an ODE directly from observations with discrete timestamps yields a spurious linear flow (Fig. 1(b)). CT-OT Flow first infers high-resolution time labels, indicated by the point colors in Fig. 1(c), and then reconstructs a continuous trajectory that matches the ground truth.

Contributions. (1) We introduce CT-OT Flow, which first applies optimal transport theory to infer high-resolution time labels (§4.3) and then uses kernel-based smoothing to generate continuous-time data distributions (§4.4). This framework allows for robust ODE/SDE estimation in scenarios where observation times are both discretized and noisy. (2) Although CT-OT Flow is formulated as a mixed-integer linear programming problem, we provide a relaxed formulation and an efficient algorithm that can solve it within practical computation times (§4.3). (3) Through numerical experiments on multiple tasks, including a real scRNA-seq dataset, we demonstrate that CT-OT Flow achieves more accurate dynamics estimation than conventional methods (§5).

2 Related work

Dynamics estimation from temporal snapshots When individual trajectories cannot be observed directly, numerous methods have been proposed for estimating dynamics from temporal snapshots [1, 2, 8, 15–21]. Neural ODE [8], Flow Matching [16], and Rectified Flow [17] represent the vector fields as neural networks, enabling learning a smooth trajectory that connects an initial distribution to a terminal one. Stochastic formulations based on SDEs and Schrödinger bridges [9] model dynamics as stochastic processes [2, 18, 19, 21–24]. To enforce smoothness across multiple time points, multi-marginal OT and spline interpolation has been explored [24, 25]. Other works estimate more realistic dynamics by adding data density-based regularization [1, 2, 19] or by constraining the trajectories to lie on the data manifold [26, 27]. However, none of these methods account for practical constraints, such as discretized time labels or uncertainty in observation times, which may limit their accuracy.

Optimal transport Optimal transport theory provides a framework for transforming one distribution into another by minimizing a chosen transport cost. In addition to defining metrics such as the Wasserstein distance [28], it has also been applied to dynamics estimation [10, 16, 20]. In particular, OT-CFM [10] employs an optimal transport approach to infer a joint distribution between two

datasets, thereby improving the learning efficiency of conditional flow matching [16]. Moreover, the relationship between the Schrödinger bridge [9] and the entropic OT problem [29] is well known [20]. However, these approaches assume that the observation times are explicitly known. Our work differs fundamentally by inferring high-resolution time label estimates for each data point, thereby accommodating discretized and noisy observation times in dynamics estimation.

Pseudotime analysis Because scRNA-seq snapshot requires destroying cells, true temporal trajectories cannot be observed directly. Pseudotime analysis methods have therefore been developed to infer an approximate ordering of cells based on their observed states [4, 12, 30–33]. For example, Monocle [31, 32] leverages geometric or graph structures in cell-state space to estimate trajectories, while RNA velocity [12] and its extension scVelo [30] predict future cell states by comparing spliced and unspliced mRNA abundances. However, these tools fall short of providing a global continuous-time model: Monocle ignores real time entirely, and RNA velocity-based ODEs are valid only over short time horizons. Moreover, neither framework adequately handles the coarse time discretization or noisy timestamps that our work directly addresses.

3 Preliminaries

3.1 Notation

Vectors are denoted by bold lowercase letters (e.g., \mathbf{a}). Let $\mathbf{1}_d$ denote the d -dimensional vector whose elements are all ones. We write $\|\cdot\|_2$ for the L^2 norm and $\delta_{\mathbf{a}}(\cdot)$ for the Dirac delta function centered at \mathbf{a} . For a set of N data points $X = \{\mathbf{x}^{(i)} \mid i = 1, \dots, N\}$, we define the corresponding empirical distribution as $\hat{p}_X = \hat{p}_X(\mathbf{x}) = \frac{1}{N} \sum_{i=1}^N \delta_{\mathbf{x}^{(i)}}(\mathbf{x})$.

3.2 Partial optimal transport

For two finite sets $X = \{\mathbf{x}^{(1)}, \dots, \mathbf{x}^{(N_x)}\}$ and $Y = \{\mathbf{y}^{(1)}, \dots, \mathbf{y}^{(N_y)}\}$, we define POT between them as

$$\text{POT}_{(\tau_x, \tau_y)}(\hat{p}_X, \hat{p}_Y) = \min_{P \in U_{(\tau_x, \tau_y)}} \sum_{i=1}^{N_x} \sum_{j=1}^{N_y} P_{ij} \|\mathbf{x}^{(i)} - \mathbf{y}^{(j)}\|_2^2, \quad (1)$$

where P is an $N_x \times N_y$ matrix with entries $P_{ij} \in [0, 1]$. The feasible set $U_{(\tau_x, \tau_y)}$ is defined by

$$U_{(\tau_x, \tau_y)} = \left\{ P \in [0, 1]^{N_x \times N_y} \mid P \mathbf{1}_{N_y} \leq \tau_x \frac{\mathbf{1}_{N_x}}{N_x}, P^\top \mathbf{1}_{N_x} \leq \tau_y \frac{\mathbf{1}_{N_y}}{N_y}, \mathbf{1}_{N_x}^\top P \mathbf{1}_{N_y} = 1 \right\}, \quad (2)$$

where $\tau_x, \tau_y \geq 1$ are scalar weights associated with the two empirical distributions. Intuitively, POT transports only a fraction $1/\tau_x$ (or $1/\tau_y$) of the total mass (see App. A for details). The 2-Wasserstein distance [28] between \hat{p}_X and \hat{p}_Y can be expressed as $\mathcal{W}(\hat{p}_X, \hat{p}_Y) = (\text{POT}_{(1,1)}(\hat{p}_X, \hat{p}_Y))^{\frac{1}{2}}$.

Link to our method. In CT-OT Flow, we solve the POT problem between two contiguous time-interval snapshots to assign each data point to high-resolution time labels.

4 Proposed method

4.1 Problem setting

Let $p_t : \mathbb{R}^d \rightarrow \mathbb{R}$, $\mathbf{x} \mapsto p_t(\mathbf{x})$ be the probability density function of the data-generating distribution at time t and $\{\mathbf{x}_t\}$ be a stochastic process on \mathbb{R}^d indexed by $\{t\}$, where $\mathbf{x}_t \sim p_t(\mathbf{x})$, and d is the dimension of the data. Consider the distribution of data observed over an interval from t to $t + \Delta t$:

$$p_{[t, t+\Delta t]}(\mathbf{x}) = \frac{1}{Z} \int_t^{t+\Delta t} p_{t'}(\mathbf{x}) p(t') dt', \quad (3)$$

where $\Delta t > 0$, $p(t')$ is the probability density function of the observation time, and Z is the normalization constant defined as $Z = \int_t^{t+\Delta t} p(t') dt'$.

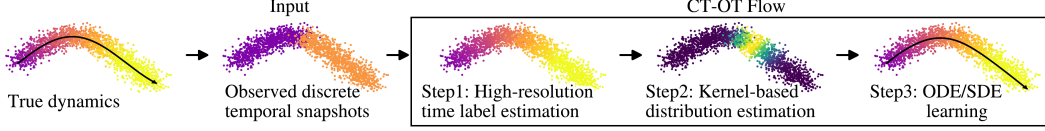


Figure 2: CT-OT Flow Pipeline: POT-based high-resolution time label estimation, kernel-based continuous-time distribution estimation, and ODE/SDE model training.

In this work, we consider *temporal snapshots* collected between discrete timestamps t_j and t_{j+1} , where $t_j < t_{j+1}$. For each $j = 1, \dots, T$, we define the temporal snapshot as

$$X_{[t_j, t_{j+1}]} = \{\mathbf{x}^{(i)} \mid \mathbf{x}^{(i)} \sim p_{[t_j, t_{j+1}]}(\mathbf{x}), i = 1, \dots, N_{[t_j, t_{j+1}]}\}, \quad (4)$$

where $N_{[t_j, t_{j+1}]} = |X_{[t_j, t_{j+1}]}|$ denotes the number of data points observed within the time interval $[t_j, t_{j+1}]$. Because the recorded observation times may be imprecise due to noise, $X_{[t_j, t_{j+1}]}$ can also include samples actually drawn from $p_{[t_j - \epsilon_t, t_{j+1} + \epsilon_t]}(\mathbf{x})$ for some $\epsilon_t > 0$.

Our goal is to recover the true continuous-time dynamics of \mathbf{x}_t by training an ODE/SDE model using temporal snapshots $X_{[t_j, t_{j+1}]}$ for $j = 1, \dots, T$. Most existing methods estimate the ODE/SDE models under the simplifying assumption that data points observed in the interval $[t_j, t_{j+1}]$ are drawn from the single time distribution $p_{t_j}(\mathbf{x})$, rather than from the aggregated distribution $p_{[t_j, t_{j+1}]}(\mathbf{x})$. As a result, the trained models can diverge substantially from the true dynamics. In contrast, our approach first estimates the distributions $p_t(\mathbf{x})$ from the temporal snapshots and then fits an ODE/SDE model, yielding a more accurate reconstruction of the underlying process.

4.2 Overview of CT-OT Flow

CT-OT Flow estimates the continuous-time distribution $p_t(\mathbf{x})$ from observed temporal snapshots and then learns an ODE/SDE from that estimated distribution. Leveraging the estimated continuous-time distribution enables capturing more precise dynamics. CT-OT Flow follows in three main steps: **(1) High-resolution time label estimation via optimal transport.** Given two contiguous temporal snapshots $X_{[t_{j-1}, t_j]}$ and $X_{[t_j, t_{j+1}]}$, CT-OT Flow uses optimal transport to infer a high-resolution time label for each data point. **(2) Kernel-based distribution estimation.** Based on the inferred high-resolution time labels, CT-OT Flow estimates a distribution $\tilde{p}_t(\mathbf{x})$ for any time t . Specifically, it applies a kernel smoothing approach in the time dimension. This step enhances robustness to noise in the recorded observation times and inaccuracies in the inferred time labels. **(3) ODE/SDE learning from the estimated distributions.** Finally, CT-OT Flow samples from the estimated distributions $\tilde{p}_t(\mathbf{x})$ and $\tilde{p}_{t+\delta t}(\mathbf{x})$, and trains a model to learn the dynamics. By choosing a small δt , we can obtain data pairs at closely spaced time points, thereby fitting an ODE/SDE at a finer temporal scale than conventional approaches, resulting in more precise dynamics. We describe these steps in detail below. Pipeline and pseudocode for CT-OT Flow are shown in Fig. 2 and Algorithm 1 in App. F, respectively.

4.3 Step 1: High-resolution time label estimation

CT-OT Flow first estimates high-resolution time labels for all data points observed in the interval $[t_j, t_{j+1}]$. Conventional methods assume that all data points in this interval belong to a single time t_j . However, in reality, each data point may have a distinct true observation time. Assuming $p_t(\mathbf{x})$ varies continuously in t , CT-OT Flow infers a high-resolution time label for each data point.

Continuity assumption Assuming $p_t(\mathbf{x})$ is continuous in t , the following holds from Eq. (3):

$$\lim_{\Delta t \rightarrow +0} p_{[t, t+\Delta t]}(\mathbf{x}) = \lim_{\Delta t \rightarrow +0} p_{[t-\Delta t, t]}(\mathbf{x}) = p_t(\mathbf{x}). \quad (5)$$

For two contiguous intervals $[t_{j-1}, t_j]$ and $[t_j, t_{j+1}]$ with $\Delta t_j, \Delta t_{j+1} > 0$, the 2-Wasserstein distance between the distributions of their subintervals $[t_j - \Delta t_j, t_j]$ and $[t_j, t_j + \Delta t_{j+1}]$ converges to zero:

$$\lim_{\Delta t_j, \Delta t_{j+1} \rightarrow +0} \mathcal{W}(p_{[t_j - \Delta t_j, t_j]}(\mathbf{x}), p_{[t_j, t_j + \Delta t_{j+1}]}(\mathbf{x})) = 0. \quad (6)$$

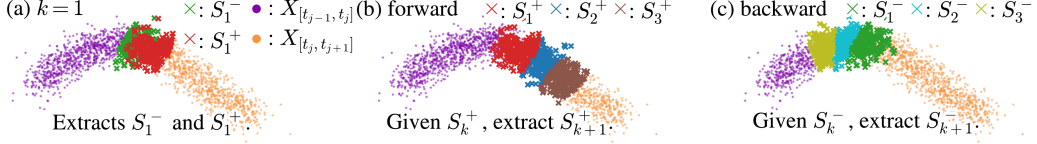


Figure 3: Step 1: high-resolution time label estimation via POT. (a) CT-OT Flow first extracts subsets S^- and S^+ near the boundary of two time intervals $X_{[t_{j-1}, t_j]}$ (purple) and $X_{[t_j, t_{j+1}]}$ (orange). (b) (Forward) CT-OT Flow iteratively identifies the subset S_{k+1}^+ . (c) (Backward) Similarly, CT-OT Flow identifies S_{k+1}^- . We set $K = 5$ to better visualize the subset extraction process.

Identifying boundary subsets Given two snapshots $X_{[t_{j-1}, t_j]}$ and $X_{[t_j, t_{j+1}]}$, CT-OT Flow identifies data points near their boundary t_j based on Eq. (6). Specifically, it finds subsets $S^- \subseteq X_{[t_{j-1}, t_j]}$ and $S^+ \subseteq X_{[t_j, t_{j+1}]}$ that capture the empirical distributions on the intervals $[t_j - \Delta t_j, t_j]$ and $[t_j, t_j + \Delta t_{j+1}]$, respectively. These subsets are estimated by solving the following optimization:

$$\min_{S^- \subseteq X_{[t_{j-1}, t_j]}, S^+ \subseteq X_{[t_j, t_{j+1}]}} \mathcal{W}^2(\hat{p}_{S^-}, \hat{p}_{S^+}) \quad \text{s.t. } |S^-| = \left\lceil \frac{N_{[t_{j-1}, t_j]}}{K} \right\rceil, |S^+| = \left\lceil \frac{N_{[t_j, t_{j+1}]}}{K} \right\rceil, \quad (7)$$

where $\lceil \cdot \rceil$ is the ceiling function, \mathcal{W}^2 is the squared 2-Wasserstein distance, and $K > 0$ is an integer.

Solving Eq. (7) extracts subsets from the two snapshots whose distributions are close in terms of the Wasserstein distance. According to Eq. (6), increasing K drives the distance between these two distributions toward zero, and thus the extracted subsets are expected to approximate $p_{t_j}(\mathbf{x})$. However, because $X_{[t_{j-1}, t_j]}$ and $X_{[t_j, t_{j+1}]}$ contain only a finite number of points, letting $K \rightarrow \infty$ trivially yields $S^- \rightarrow \emptyset$ and $S^+ \rightarrow \emptyset$. Hence, in practice, we fix a finite K so as to estimate the data points in the contiguous intervals $[t_j - \Delta t_j, t_j]$ and $[t_j, t_j + \Delta t_{j+1}]$. Our preliminary experiments indicate that tuning K suitably allows for a robust extraction of these subsets; see App. B for more details. Figure 3 (a) shows an example of S^- and S^+ identified by CT-OT Flow.

Mixed-Integer Linear Programming relaxation The optimization problem in Eq. (7) is a mixed-integer linear programming (MILP). As the dataset size grows, the computational cost escalates, making it increasingly difficult to solve directly. Therefore, instead of solving Eq. (7) exactly, CT-OT Flow adopts a continuous relaxation of the problem, formulated as follows:

$$\min_{P \in U_{(K, K)}} \sum_{m=1}^{N_{[t_{j-1}, t_j]}} \sum_{n=1}^{N_{[t_j, t_{j+1}]}} P_{m,n} \|\mathbf{x}^{(m)} - \mathbf{x}^{(n)}\|_2^2, \quad (8)$$

where $\mathbf{x}^{(m)} \in X_{[t_{j-1}, t_j]}$ and $\mathbf{x}^{(n)} \in X_{[t_j, t_{j+1}]}$.

Proposition 1. *The problem in Eq. (8) is the continuous relaxation of the MILP in Eq. (7).*

A proof is provided in App. E.

Eq. (8) is a POT problem, $\text{POT}_{(K, K)}(\hat{p}_{X_{[t_{j-1}, t_j]}}, \hat{p}_{X_{[t_j, t_{j+1}]}})$, so its optimal plan P^* provides a *soft* matching between the two snapshots and can be computed within a practical time. To obtain hard subsets of the desired size, we sort all points by their row (or column) sums in P^* and retain exactly $\lceil N_{[t_{j-1}, t_j]} / K \rceil$ (or $\lceil N_{[t_j, t_{j+1}]} / K \rceil$) points on the first (or second) snapshot. In this way we keep only those samples that participate *most strongly* in the optimal transport, simultaneously satisfying the cardinality constraint and concentrating on points that lie closest to the interval boundary.

Iterative extraction of subsets CT-OT Flow then iteratively applies the similar procedure to identify subsets in each contiguous time sub-interval. Specifically, for $k = 1, \dots, K - 2$, we iteratively identify the subsets $S_{k+1}^- \subset X_{[t_{j-1}, t_j]}$ (backward) and $S_{k+1}^+ \subset X_{[t_j, t_{j+1}]}$ (forward) as follows.

$$\min_{S_{k+1}^- \subset X_{[t_{j-1}, t_j]} \setminus (\cup_{k'=1}^k S_{k'}^-)} \mathcal{W}^2(\hat{p}_{S_{k+1}^-}, \hat{p}_{S_{k+1}^-}) \quad \text{s.t. } |S_{k+1}^-| = \left\lceil \frac{N_{[t_{j-1}, t_j]}}{K} \right\rceil \quad (\text{backward}), \quad (9)$$

$$\min_{S_{k+1}^+ \subset X_{[t_j, t_{j+1}]} \setminus (\cup_{k'=1}^k S_{k'}^+)} \mathcal{W}^2(\hat{p}_{S_{k+1}^+}, \hat{p}_{S_{k+1}^+}) \quad \text{s.t. } |S_{k+1}^+| = \left\lceil \frac{N_{[t_j, t_{j+1}]}}{K} \right\rceil \quad (\text{forward}), \quad (10)$$

where $S_1^- = S^-$, $S_1^+ = S^+$. By applying the same relaxation as in Eq. (7), each step can be solved via POT. See App. E for details. For $k = K$, we take $S_K^- = X_{[t_{j-1}, t_j]} \setminus \cup_{k=1}^{K-1} S_k^-$ and $S_K^+ = X_{[t_j, t_{j+1}]} \setminus \cup_{k=1}^{K-1} S_k^+$. Here, we expect S_{k+1}^- and S_k^- (and S_{k+1}^+ and S_k^+) to correspond to temporally contiguous subsets. Figures 3 (b) and (c) illustrate examples of S_k^- and S_k^+ . In CT-OT Flow, the subsets are thus extracted step-by-step from each boundary, moving backward and forward.

High-resolution time labels Through the above procedure, each of $X_{[t_{j-1}, t_j]}$ and $X_{[t_j, t_{j+1}]}$ is partitioned into K subsets. We then assign high-resolution time labels to each data point $\mathbf{x}^{(i)}$ according to the subsets. If the sampling density $p(t)$ inside each coarse interval is known (e.g., from experimental design), high-resolution time labels can be obtained via the inverse CDF:

$$\tilde{t}_-^{(i)} = F_{-,j}^{-1}\left(\frac{k}{K+1}\right) \in [t_{j-1}, t_j], \text{ if } \mathbf{x}^{(i)} \in S_k^- \subset X_{[t_{j-1}, t_j]} \text{ (backward),} \quad (11)$$

$$\tilde{t}_+^{(i)} = F_{+,j}^{-1}\left(\frac{k}{K+1}\right) \in [t_j, t_{j+1}], \text{ if } \mathbf{x}^{(i)} \in S_k^+ \subset X_{[t_j, t_{j+1}]} \text{ (forward),} \quad (12)$$

where $F_{-,j}(t) = \frac{1}{Z_{-,j}} \int_t^{t_j} p(t') dt'$ and $F_{+,j}(t) = \frac{1}{Z_{+,j}} \int_{t_j}^t p(t') dt'$, and $F_{-,j}^{-1}$ and $F_{+,j}^{-1}$ are their inverse functions. $Z_{+,j} = \int_{t_j}^{t_{j+1}} p(t') dt'$ and $Z_{-,j} = \int_{t_{j-1}}^{t_j} p(t') dt'$ are normalization constants.

Hence, each data point is assigned a high-resolution time label $\tilde{t}^{(i)} = \tilde{t}_-^{(i)}$ (or $\tilde{t}_+^{(i)}$). Applying this procedure to every pair of contiguous intervals in $\{X_{[t_j, t_{j+1}]} \}_{j=1}^T$ yields high-resolution time labels. If a point is assigned both $\tilde{t}_-^{(i)}$ and $\tilde{t}_+^{(i)}$, we take their average as the final estimate.

When the true observation-time distribution $p(t)$ is unknown, we simply assume it to be **uniform within each coarse interval** (see App. D for the non-uniform case). In the following, we focus on the uniform scenario. Although CT-OT Flow is derived for contiguous intervals, it can also be applied to non-contiguous pairs and often still yields reliable high-resolution time labels (see §5 and App. I).

4.4 Step 2: Estimating data distribution in continuous time

Using the high-resolution time labels $\tilde{t}^{(i)}$, CT-OT Flow constructs the data distribution at any time t . Specifically, we define the *kernel-based time-smoothed empirical distribution* at time t :

$$\tilde{p}_t(\mathbf{x}) = \frac{1}{Z_{\text{kernel}}(t)} \sum_{i=1}^{|X|} k(t, \tilde{t}^{(i)}) \delta_{\mathbf{x}^{(i)}}(\mathbf{x}), \quad (13)$$

where $X = \cup_{j=1}^T X_{[t_j, t_{j+1}]}$ denotes the set of all data points, $Z_{\text{kernel}}(t) = \sum_{i=1}^{|X|} k(t, \tilde{t}^{(i)})$, and $k(t, \tilde{t}^{(i)})$ is a kernel function. For example, we can use the Gaussian kernel $k(t, \tilde{t}^{(i)}) = \exp(-|t - \tilde{t}^{(i)}|^2/\gamma)$, where $\gamma > 0$ controls the degree of smoothing.

This approach yields a robust estimate of the distribution under temporal noise. In particular, data points near interval boundaries (e.g., around t_j) may be assigned to different time intervals if observation times are noisy. By smoothing along the *time axis*, the estimator becomes tolerant to both high-resolution time label errors and measurement noise. Note that this smoothing is applied in the temporal dimension, unlike smoothing in the feature space, such as in kernel density estimation [34]. In App. C, we demonstrate the effect of γ on $p_t(\mathbf{x})$.

4.5 Step 3: Dynamics estimation

CT-OT Flow then estimates the dynamics using $\tilde{p}_t(\mathbf{x})$ from Step 2. Specifically, we draw paired samples from $\tilde{p}_t(\mathbf{x})$ and $\tilde{p}_{t+\delta t}(\mathbf{x})$ for $\delta t > 0$, and fit an ODE/SDE model to them. A key advantage of CT-OT Flow is that δt can be chosen arbitrarily small, allowing more realistic dynamics estimation, whereas conventional methods rely on a fixed set of discrete time points. Figure 4 shows an example with $t = 2.0$ and $\delta t = 0.3$, where the time intervals of the inputs are $[1, 2]$ and $[2, 3]$.

CT-OT Flow can be combined with existing ODE/SDE models. For instance, Rectified Flow [17] models the velocity field with a neural network $\mathbf{v}_\theta(\mathbf{x}_t, t)$. Let $\mathbf{x}^{(0)}$ and $\mathbf{x}^{(1)}$ be samples from $\tilde{p}_t(\mathbf{x})$ and $\tilde{p}_{t+\delta t}(\mathbf{x})$, respectively. Their velocity vector is estimated as $\frac{\mathbf{x}^{(1)} - \mathbf{x}^{(0)}}{\delta t}$. We adapt the Rectified

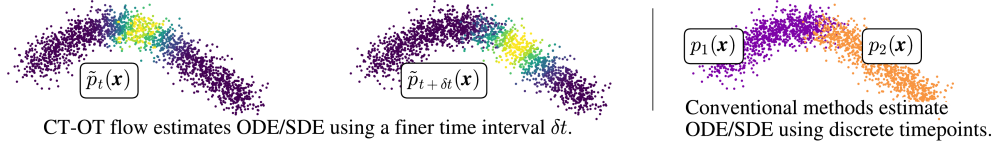


Figure 4: Steps 2&3. A kernel function produces a smoothed empirical distribution $\tilde{p}_t(\mathbf{x})$ at any continuous time t . We then sample from \tilde{p}_t and $\tilde{p}_{t+\delta t}$ to train a dynamics model. Unlike conventional methods that operate only on pre-specified discrete times, CT-OT Flow allows arbitrarily fine choices of δt , capturing more realistic trajectories.

Flow loss to our framework as follows:

$$\mathcal{L}_{\text{RF}} = \mathbb{E}_{(\mathbf{x}^{(0)}, \mathbf{x}^{(1)}, t, t') \sim Q} \left[\left\| \frac{\mathbf{x}^{(1)} - \mathbf{x}^{(0)}}{\delta t} - \mathbf{v}_\theta(t' \mathbf{x}^{(1)} + (1 - t') \mathbf{x}^{(0)}, t + t' \delta t) \right\|_2^2 \right], \quad (14)$$

where $Q = \tilde{p}_t(\mathbf{x}) \otimes \tilde{p}_{t+\delta t}(\mathbf{x}) \otimes \mathcal{U}(t|t_1, t_{T+1} - \delta t) \otimes \mathcal{U}(t'|0, 1)$, \mathcal{U} is a uniform distribution, and \otimes denotes the product of probability distributions. Thanks to CT-OT Flow, the time variable t is sampled from a *continuous* range rather than a discrete set. Thus, CT-OT Flow enables learning dynamics from a continuous temporal perspective. Similarly, our framework can be integrated with methods such as conditional flow matching [10] or [SF]²M [2] for ODE/SDE estimation.

4.6 Computational cost

The overall runtime of CT-OT Flow depends on three parameters: the number of intervals T , the number of samples per interval N , and the subdivision factor K . We denote by $C(M, N)$ the cost of solving a single POT instance of size $M \times N$. While the network simplex algorithm has worst-case super-cubic complexity [35], the Sinkhorn iteration runs in $O(MN)$ time per iteration [29].

(Step 1.) For $k = 1$, we solve one POT problem for each of the T snapshot pairs, costing $TC(N, N)$. For each subsequent level $k = 2, \dots, K - 1$ we solve two POT problems (backward and forward) between a block of $\frac{N}{K}$ points and the remaining $\frac{N(K-k+1)}{K}$ points. This incurs an additional cost of $2T \sum_{k=2}^{K-1} C(\frac{N}{K}, \frac{N(K-k+1)}{K})$. One practical acceleration splits each interval’s points into $\frac{N}{m}$ random mini-batches of size m , runs CT-OT Flow independently on $\frac{N}{m}$ batch pairs, and then concatenates the resulting high-resolution time labels. With fixed m , the cost of Step 1 scales linearly in N . Here, m trades off accuracy (large m preserves global structure) and computation (small m is faster).

(Step 2.) Kernel smoothing over the T intervals requires $O(TN)$ time.

(Step 3.) The cost matches that of the downstream ODE/SDE learner (e.g. Rectified Flow [17]).

On a single CPU thread using network simplex, Step 1 takes approximately 70 seconds for $N = 10^4$, $T = 1$, $K = 100$. Under a mini-batch setup with $m = 10^3$, the runtimes are approximately 3 seconds, 30 seconds, and 400 seconds for $N = 10^4$, 10^5 , and 10^6 , respectively. Note that these computation times are shorter than those of the neural network training phase in existing methods or Step 3, which can range from minutes to hours. See App. G for details on computation times when varying N and K , as well as the mini-batch approach.

5 Experiments

We evaluate the performance of CT-OT Flow through numerical experiments. First, we describe the evaluation metrics in §5.1. Next, in §5.2, we assess how well each method recovers the true dynamics using synthetic data. Finally, we present an application to real scRNA-seq data and meteorological data in §5.3 and §5.4, respectively. For these experiments, we compare CT-OT Flow against recent methods, including ODE-based approaches such as I-CFM, OT-CFM [10], TrajectoryNet-Base [1], and Metric Flow Matching (MFM) [26], as well as SDE-based approaches such as [SF]²M-I, [SF]²M-Exact [2] and Entropic Neural Optimal Transport (ENOT) [20]. We combine CT-OT Flow with OT-CFM [10] to estimate ODEs and with [SF]²M-Exact [2] to estimate SDEs. We use a Gaussian kernel with parameter $\gamma = 0.005$ for Step 2, and the subdivision factor is set to $K = 100$ for all datasets unless otherwise stated. Performance sensitivity to K and γ is examined in App. B and App. C, respectively. Additional experimental parameters are listed in App. H.

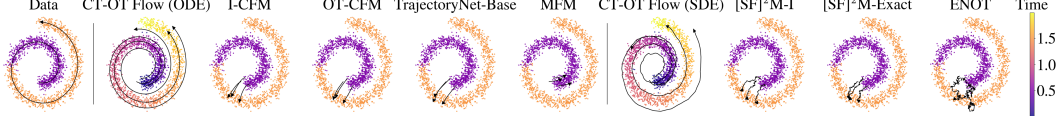


Figure 5: Estimated trajectories on the Spiral dataset. The black lines indicate the true or estimated trajectories, while the color of each point indicates its (high-resolution) time label. The initial points are sampled from $p_0(\mathbf{x})$ but not from $p_{[0,1]}(\mathbf{x})$. The proposed method effectively reproduces the true dynamics, whereas conventional methods often yield larger deviations from the ground truth.

5.1 Evaluation metrics

When the true dynamics are known (i.e., when the true data distribution $p_t^*(\mathbf{x})$ at each time t and the corresponding ODE/SDE describing the movement of data points are available) we evaluate each method by comparing the trajectories derived from the true dynamics to the estimated trajectories. We assume that the true system produces trajectories $X_j^* = [\mathbf{x}_{j,0}^*, \dots, \mathbf{x}_{j,T^*}^*]$ for $j = 1, \dots, N^*$, where T^* is the number of time steps and $\mathbf{x}_{j,0}^*$ denotes the mean of the true initial distribution $p_0^*(\mathbf{x})$. Each model produces an estimated trajectory $\hat{X}^{(i)} = [\hat{\mathbf{x}}_0^{(i)}, \dots, \hat{\mathbf{x}}_{\hat{T}_i}^{(i)}]$, where \hat{T}_i is the number of simulated time steps and $i = 1, \dots, \hat{N}$; the initial point $\hat{\mathbf{x}}_0^{(i)}$ is drawn from $p_0^*(\mathbf{x})$ (not from $p_{[0,1]}(\mathbf{x})$).

We employ two metrics to evaluate the accuracy of the estimated dynamics. The first metric quantifies the discrepancy between the true and estimated trajectories using Dynamic Time Warping [36]:

$$\mathcal{L}_{\text{DTW}} = \frac{1}{\hat{N}} \sum_{i=1}^{\hat{N}} \min_j \text{DTW}(X_j^*, \hat{X}^{(i)}) \quad (15)$$

The second metric computes the average 1-Wasserstein distance [28] between the true distribution $p_t^*(\mathbf{x})$ and the distribution estimated from the simulated trajectories:

$$\mathcal{L}_{\text{Wass}} = \frac{1}{T^*} \sum_{t=1}^{T^*} \mathcal{W}_1(\hat{p}_{\hat{\mathbf{x}}_{t'}}, p_t^*(\mathbf{x})), \text{ where } t' = \left\lfloor t \frac{\hat{T}_i}{T^*} \right\rfloor, \hat{\mathbf{x}}_{t'} = \{\hat{\mathbf{x}}_{t'}^{(i)}\}_{i=1}^{\hat{N}}. \quad (16)$$

Here, $\lfloor \cdot \rfloor$ represents the floor function and \mathcal{W}_1 is the 1-Wasserstein distance [28].

5.2 Synthetic data experiments

We evaluate dynamics estimation methods using three synthetic datasets; Spiral, Y-shaped, and Arch [26]. For Spiral and Y-shaped, data are collected over two contiguous time intervals, while the Arch dataset comprises data from two non-contiguous intervals. See App. J for details.

Figure 5 shows estimated trajectories for the Spiral dataset, while Fig. 17 in App. K shows those for the Y-shaped and Arch datasets. In these figures, the colors of the points indicate discrete time intervals, and for CT-OT Flow, the color of each point reflects its high-resolution time label. Table 1 summarizes the mean and standard deviation of the metrics over 10 runs with different neural network initializations. Boldface marks the best mean within each ODE/SDE group, while \dagger denotes results significantly better than all baselines ($p < 0.05$, two-sided independent t -test).

These results indicate that CT-OT Flow recovers trajectories that are closer to the true dynamics than those yielded by conventional methods for both the Spiral and Y-shaped datasets, owing to its consideration of discretized times and time uncertainty. Moreover, even for the Arch dataset, where the observed intervals are non-contiguous, our method achieves accuracy comparable to that of MFM [26] in predicting the trajectories. See App. I for additional evaluation on data with non-contiguous intervals. We further examine the effect of omitting steps of CT-OT Flow in App. K.3.

5.3 Application to scRNA-seq data

In this section, we evaluate CT-OT Flow on real scRNA-seq data. We generate time-discretized datasets from the Bifurcation dataset [37, 33] and embryoid body (EB) dataset [11] by grouping the first three (for Bifurcation) or two (for EB) time points as one interval and the next three as a second

Table 1: Estimation errors (mean \pm std) on the synthetic datasets. Bold: best within ODE/SDE groups; †: statistically significant vs. baselines ($p < 0.05$).

Dataset \rightarrow Method \downarrow Metric \rightarrow	Spiral		Y-shaped		Arch	
	\mathcal{L}_{DTW}	\mathcal{L}_{Wass}	\mathcal{L}_{DTW}	\mathcal{L}_{Wass}	\mathcal{L}_{DTW}	\mathcal{L}_{Wass}
CT-OT Flow (ODE)	9.64 \pm 1.04 [†]	0.31 \pm 0.04 [†]	10.79 \pm 0.66 [†]	0.41 \pm 0.10 [†]	9.98 \pm 2.88 [†]	0.31 \pm 0.08
I-CFM [10]	50.57 \pm 0.18	1.11 \pm 0.01	21.76 \pm 0.53	0.61 \pm 0.02	29.07 \pm 0.31	0.58 \pm 0.01
OT-CFM [10]	51.41 \pm 0.02	1.17 \pm 0.00	29.41 \pm 0.17	0.90 \pm 0.00	31.68 \pm 0.12	0.62 \pm 0.00
TrajectoryNet [1]	51.65 \pm 0.14	1.19 \pm 0.03	21.93 \pm 6.07	0.89 \pm 0.07	33.82 \pm 2.53	0.68 \pm 0.08
MFM [26]	45.70 \pm 0.04	1.11 \pm 0.00	43.43 \pm 0.21	1.24 \pm 0.07	13.53 \pm 1.53	0.31 \pm 0.02
CT-OT Flow (SDE)	11.66 \pm 1.06 [†]	0.36 \pm 0.04 [†]	11.47 \pm 0.78 [†]	0.45 \pm 0.09 [†]	11.43 \pm 2.60 [†]	0.34 \pm 0.08 [†]
[SF] ² M-I [2]	49.98 \pm 0.19	1.11 \pm 0.01	21.44 \pm 0.51	0.61 \pm 0.01	28.29 \pm 0.25	0.58 \pm 0.00
[SF] ² M-Exact [2]	51.33 \pm 0.04	1.17 \pm 0.01	28.99 \pm 0.18	0.89 \pm 0.00	31.01 \pm 0.16	0.62 \pm 0.00
ENOT [20]	49.59 \pm 0.05	1.15 \pm 0.00	25.98 \pm 0.26	0.82 \pm 0.01	24.48 \pm 0.22	0.57 \pm 0.00

interval, yielding two-interval datasets for training. Bifurcation data are four-dimensional, while EB data are two-dimensional (see App. J for details).

After training on the time-discretized dataset, we evaluate each method by simulating trajectories on the held-out test data, starting from samples at the earliest original time point. Since true dynamics are unknown, we treat the empirical distribution at each original time point as ground truth and report \mathcal{L}_{Wass} . Table 2 summarizes the evaluation scores over 10 runs. As shown in Tab. 2, CT-OT Flow achieves highly accurate reconstruction of time-evolving data distributions from the temporal snapshots. Figure 17 in App. K further illustrates the predicted trajectories.

5.4 Application to meteorological data

Finally, we evaluate CT-OT Flow on 528 typhoon trajectories recorded in Southeast Asia between 1951 and 2024. We split the data 70%/30% for training and testing sets and use snapshots at genesis (0 h), 72 h, and 144 h. Performance is measured using \mathcal{L}_{DTW} and \mathcal{L}_{Wass} . CT-OT Flow (ODE) significantly reduces \mathcal{L}_{DTW} from 17.16 \pm 0.07 to 16.59 \pm 0.25 and \mathcal{L}_{Wass} from 0.48 \pm 0.01 to 0.35 \pm 0.05 over the baseline, demonstrating its effectiveness on meteorological trajectory data. See App. K.2 for further details.

6 Conclusions and Limitations

We introduced CT-OT Flow, a general framework that leverages POT to assign high-resolution time labels from discrete temporal snapshots and build a continuous-time data distribution, enabling more accurate reconstruction of underlying dynamics. Our experiments on both synthetic and real-world datasets show that CT-OT Flow outperforms existing methods. These improvements result from explicitly modeling temporal discretization and timestamp uncertainty.

Limitations: First, CT-OT Flow relies on the observation-time distribution $p(t)$ in Eqs. (11) and (12). When $p(t)$ is unavailable, we assume it to be uniform over each coarse interval. While this simplification makes the method tractable, it introduces systematic bias in the estimated velocity magnitude when the true $p(t)$ deviates from uniformity (see App. D). A promising avenue for future work is to jointly infer $p(t)$ from external cues such as RNA velocity [12]. Second, in high-dimensional settings, the pairwise distances between data points tend to concentrate, impairing the ability to accurately distinguish those near temporal boundaries. We found that increasing the kernel smoothing parameter γ alleviates this issue (see App. K.4). Additionally, mapping to a lower-dimensional space may enable the effective identification of points near boundaries even when dealing with high-dimensional data. These limitations highlight areas for future improvement and extension of CT-OT Flow.

Table 2: Estimation errors (\mathcal{L}_{Wass}) on the scRNA-seq datasets. Bold: best within ODE/SDE groups; †: statistically significant vs. baselines ($p < 0.05$).

Method \downarrow Dataset \rightarrow	Bifurcation	EB
CT-OT Flow (ODE)	0.64 \pm 0.04	0.94 \pm 0.11
I-CFM [10]	0.71 \pm 0.00	1.00 \pm 0.01
OT-CFM [10]	0.70 \pm 0.00	1.06 \pm 0.01
TrajectoryNet [1]	0.68 \pm 0.04	1.11 \pm 0.04
MFM [26]	0.69 \pm 0.01	1.03 \pm 0.05
CT-OT Flow (SDE)	0.63 \pm 0.04 [†]	0.92 \pm 0.12
[SF] ² M-I [2]	0.71 \pm 0.00	0.99 \pm 0.01
[SF] ² M-Exact [2]	0.71 \pm 0.01	1.06 \pm 0.01
ENOT [20]	0.70 \pm 0.01	1.02 \pm 0.02

References

- [1] Alexander Tong, Jessie Huang, Guy Wolf, David van Dijk, and Smita Krishnaswamy. Trajectory-rynet: A dynamic optimal transport network for modeling cellular dynamics. In *Proceedings of the 37th International Conference on Machine Learning*, 2020.
- [2] Alexander Y Tong, Nikolay Malkin, Kilian Fatras, Lazar Atanackovic, Yanlei Zhang, Guillaume Huguët, Guy Wolf, and Yoshua Bengio. Simulation-free Schrödinger bridges via score and flow matching. In *International Conference on Artificial Intelligence and Statistics*, pages 1279–1287. PMLR, 2024.
- [3] Haifeng Niu and Elisabete A Silva. Understanding temporal and spatial patterns of urban activities across demographic groups through geotagged social media data. *Computers, Environment and Urban Systems*, 100:101934, 2023.
- [4] Charlotte Bunne, Stefan G Stark, Gabriele Gut, Jacobo Sarabia Del Castillo, Mitch Levesque, Kjong-Van Lehmann, Lucas Pelkmans, Andreas Krause, and Gunnar Rätsch. Learning single-cell perturbation responses using neural optimal transport. *Nature methods*, 20(11):1759–1768, 2023.
- [5] Grace XY Zheng, Jessica M Terry, Phillip Belgrader, Paul Ryvkin, Zachary W Bent, Ryan Wilson, Solongo B Ziraldo, Tobias D Wheeler, Geoff P McDermott, Junjie Zhu, et al. Massively parallel digital transcriptional profiling of single cells. *Nature communications*, 8(1):14049, 2017.
- [6] Yu Zheng, Licia Capra, Ouri Wolfson, and Hai Yang. Urban computing: Concepts, methodologies, and applications. *ACM Trans. Intell. Syst. Technol.*, 5(3), September 2014. ISSN 2157-6904. doi: 10.1145/2629592.
- [7] Jennifer Yick, Biswanath Mukherjee, and Dipak Ghosal. Wireless sensor network survey. *Computer networks*, 52(12):2292–2330, 2008.
- [8] Ricky T. Q. Chen, Yulia Rubanova, Jesse Bettencourt, and David K Duvenaud. Neural ordinary differential equations. In S. Bengio, H. Wallach, H. Larochelle, K. Grauman, N. Cesa-Bianchi, and R. Garnett, editors, *Advances in Neural Information Processing Systems*, volume 31. Curran Associates, Inc., 2018.
- [9] Christian Léonard. A survey of the Schrödinger problem and some of its connections with optimal transport. *arXiv preprint arXiv:1308.0215*, 2013.
- [10] Alexander Tong, Kilian FATRAS, Nikolay Malkin, Guillaume Huguët, Yanlei Zhang, Jarrod Rector-Brooks, Guy Wolf, and Yoshua Bengio. Improving and generalizing flow-based generative models with minibatch optimal transport. *Transactions on Machine Learning Research*, 2024.
- [11] Kevin Moon. Embryoid body data for PHATE. *Mendeley Data*, 1, 2018.
- [12] Gioele La Manno, Ruslan Soldatov, Amit Zeisel, Emelie Braun, Hannah Hochgerner, Viktor Petukhov, Katja Lidschreiber, Maria E Kastriti, Peter Lönnerberg, Alessandro Furlan, et al. Rna velocity of single cells. *Nature*, 560(7719):494–498, 2018.
- [13] Nicolas Bonneel and David Coeurjolly. Spot: sliced partial optimal transport. *ACM Trans. Graph.*, 38(4), July 2019. ISSN 0730-0301. doi: 10.1145/3306346.3323021.
- [14] Alessio Figalli. The optimal partial transport problem. *Archive for rational mechanics and analysis*, 195(2):533–560, 2010.
- [15] Martin Rohbeck, Charlotte Bunne, Edward De Brouwer, Jan-Christian Huetter, Anne Biton, Kelvin Y. Chen, Aviv Regev, and Romain Lopez. Modeling complex system dynamics with flow matching across time and conditions. In *The Thirteenth International Conference on Learning Representations*, 2025.
- [16] Yaron Lipman, Ricky TQ Chen, Heli Ben-Hamu, Maximilian Nickel, and Matt Le. Flow matching for generative modeling. In *11th International Conference on Learning Representations, ICLR 2023*, 2023.

- [17] Xingchao Liu, Chengyue Gong, and Qiang Liu. Flow straight and fast: Learning to generate and transfer data with rectified flow. In *The Eleventh International Conference on Learning Representations (ICLR)*, 2023.
- [18] Alexander Korotin, Nikita Gushchin, and Evgeny Burnaev. Light Schrödinger bridge. *arXiv preprint arXiv:2310.01174*, 2023.
- [19] Takeshi Koshizuka and Issei Sato. Neural lagrangian Schrödinger bridge: Diffusion modeling for population dynamics. *arXiv preprint arXiv:2204.04853*, 2022.
- [20] Nikita Gushchin, Alexander Kolesov, Alexander Korotin, Dmitry P Vetrov, and Evgeny Burnaev. Entropic neural optimal transport via diffusion processes. *Advances in Neural Information Processing Systems*, 36, 2024.
- [21] Dominik Klein, Théo Uscidda, Fabian Theis, and Marco Cuturi. GENOT: Entropic (Gromov) Wasserstein flow matching with applications to single-cell genomics. *Advances in Neural Information Processing Systems*, 37:103897–103944, 2024.
- [22] Yang Song, Jascha Sohl-Dickstein, Diederik P Kingma, Abhishek Kumar, Stefano Ermon, and Ben Poole. Score-based generative modeling through stochastic differential equations. In *International Conference on Learning Representations*, 2021.
- [23] Kirill Neklyudov, Rob Brekelmans, Daniel Severo, and Alireza Makhzani. Action matching: Learning stochastic dynamics from samples. In *International conference on machine learning*, pages 25858–25889. PMLR, 2023.
- [24] Tianrong Chen, Guan-hong Liu, Molei Tao, and Evangelos A Theodorou. Deep multi-marginal momentum Schrödinger bridge. In *Proceedings of the 37th International Conference on Neural Information Processing Systems*, pages 57058–57086, 2023.
- [25] Justin Lee, Behnaz Moradijamei, and Heman Shakeri. Multi-marginal stochastic flow matching for alignment of high-dimensional snapshot data at irregular time points, 2025.
- [26] Kacper Kapusniak, Peter Potaptchik, Teodora Reu, Leo Zhang, Alexander Tong, Michael Bronstein, Avishek Joey Bose, and Francesco Di Giovanni. Metric flow matching for smooth interpolations on the data manifold. *arXiv preprint arXiv:2405.14780*, 2024.
- [27] Ricky TQ Chen and Yaron Lipman. Flow matching on general geometries. *arXiv preprint arXiv:2302.03660*, 2023.
- [28] Gabriel Peyré, Marco Cuturi, et al. Computational optimal transport: With applications to data science. *Foundations and Trends® in Machine Learning*, 11(5-6):355–607, 2019.
- [29] Marco Cuturi. Sinkhorn distances: Lightspeed computation of optimal transport. In C.J. Burges, L. Bottou, M. Welling, Z. Ghahramani, and K.Q. Weinberger, editors, *Advances in Neural Information Processing Systems*, volume 26. Curran Associates, Inc., 2013.
- [30] Volker Bergen, Marius Lange, Stefan Peidli, F. Alexander Wolf, and Fabian J. Theis. Generalizing rna velocity to transient cell states through dynamical modeling. *Nature Biotechnology*, 38(12):1408–1414, August 2020. ISSN 1546-1696. doi: 10.1038/s41587-020-0591-3.
- [31] Cole Trapnell, Davide Cacchiarelli, Jonna Grimsby, Prapti Pokharel, Shuqiang Li, Michael Morse, Niall J Lennon, Kenneth J Livak, Tarjei S Mikkelsen, and John L Rinn. The dynamics and regulators of cell fate decisions are revealed by pseudotemporal ordering of single cells. *Nature biotechnology*, 32(4):381–386, 2014.
- [32] Xiaojie Qiu, Qi Mao, Ying Tang, Li Wang, Raghav Chawla, Hannah A Pliner, and Cole Trapnell. Reversed graph embedding resolves complex single-cell trajectories. *Nature methods*, 14(10): 979–982, 2017.
- [33] Yutong Sha, Yuchi Qiu, Peijie Zhou, and Qing Nie. Reconstructing growth and dynamic trajectories from single-cell transcriptomics data. *Nature Machine Intelligence*, 6(1):25–39, 2024.

- [34] SILVERMAN BW. Density estimation for statistics and data analysis. *Monographs on Statistics and Applied Probability*, 1986.
- [35] Ravindra K Ahuja, Thomas L Magnanti, James B Orlin, et al. *Network flows: theory, algorithms, and applications*, volume 1. Prentice hall Englewood Cliffs, NJ, 1993.
- [36] Hiroaki Sakoe and Seibi Chiba. Dynamic programming algorithm optimization for spoken word recognition. *IEEE transactions on acoustics, speech, and signal processing*, 26(1):43–49, 1978.
- [37] Rhishikesh Bargaje, Kalliopi Trachana, Martin N. Shelton, Christopher S. McGinnis, Joseph X. Zhou, Cora Chadick, Savannah Cook, Christopher Cavanaugh, Sui Huang, and Leroy Hood. Cell population structure prior to bifurcation predicts efficiency of directed differentiation in human induced pluripotent cells. *Proceedings of the National Academy of Sciences*, 114(9): 2271–2276, 2017. doi: 10.1073/pnas.1621412114.
- [38] Rémi Flamary, Nicolas Courty, Alexandre Gramfort, Mokhtar Z Alaya, Aurélie Boissunon, Stanislas Chambon, Laetitia Chapel, Adrien Corenflos, Kilian Fatras, Nemo Fournier, et al. Pot: Python optimal transport. *Journal of Machine Learning Research*, 22(78):1–8, 2021.
- [39] Günter Klambauer, Thomas Unterthiner, Andreas Mayr, and Sepp Hochreiter. Self-normalizing neural networks. In I. Guyon, U. Von Luxburg, S. Bengio, H. Wallach, R. Fergus, S. Vishwanathan, and R. Garnett, editors, *Advances in Neural Information Processing Systems*, volume 30. Curran Associates, Inc., 2017.
- [40] Diederik P Kingma and Jimmy Ba. Adam: A method for stochastic optimization. *arXiv preprint arXiv:1412.6980*, 2014.
- [41] I Loshchilov. Decoupled weight decay regularization. *arXiv preprint arXiv:1711.05101*, 2017.
- [42] Kevin R Moon, David Van Dijk, Zheng Wang, Scott Gigante, Daniel B Burkhardt, William S Chen, Kristina Yim, Antonia van den Elzen, Matthew J Hirn, Ronald R Coifman, et al. Visualizing structure and transitions in high-dimensional biological data. *Nature biotechnology*, 37(12):1482–1492, 2019.

A Background of partial optimal transport

In this section, we provide a formulation of optimal transport between two empirical distributions that consist of distinct sets of data points, with a particular focus on POT [13, 14], which is used in this work. Optimal transport seeks a coupling between two distributions that minimizes a given cost function. Let two finite point sets be $X = \{\mathbf{x}^{(1)}, \dots, \mathbf{x}^{(N_x)}\}$ and $Y = \{\mathbf{y}^{(1)}, \dots, \mathbf{y}^{(N_y)}\}$. Here, N_x, N_y are the respective number of data points, and $\mathbf{x}^{(i)}, \mathbf{y}^{(j)} \in \mathbb{R}^d$ for all i, j .

Let \hat{p}_X and \hat{p}_Y be the empirical distributions corresponding to X and Y , respectively. Depending on the values of τ_x and τ_y , different optimal transport regimes emerge for $\text{POT}_{(\tau_x, \tau_y)}(\hat{p}_X, \hat{p}_Y)$:

1. ($\tau_x = \tau_y = 1$). Full OT: all mass in X and Y is transported.
2. ($\tau_x > \tau_y = 1$). One-sided POT: only a fraction $\frac{1}{\tau_x}$ of the total mass in X is transported to the entirety of Y .
3. ($\tau_y > \tau_x = 1$). One-sided POT: only a fraction $\frac{1}{\tau_y}$ of the total mass in Y is transported to the entirety of X .
4. ($\tau_x = \tau_y > 1$). Two-sided POT: only subsets of points from both X, Y are transported.

B Effect of the subdivision factor K

In this section, we examine how the inferred high-resolution time labels change as the subdivision factor K in CT-OT Flow varies. Figure 6 illustrates the high-resolution time label estimated for the three synthetic datasets used in §5.2, under different values of K . Figure 7 shows the Spearman’s rank correlation coefficients between the inferred times and the true times, averaged over 10 runs with different random seeds for data generation. If K is small, the time resolution is coarse, resulting in a weaker correlation between the inferred and true times. As K increases, the time resolution gradually improves and the correlation coefficient increases accordingly. However, if K becomes excessively large, the noise in the data exerts a greater influence on the time estimates, and estimation accuracy gradually degrades. Hence, rather than taking $K \rightarrow \infty$, choosing an appropriate value of K enables one to achieve high-accuracy estimation of the true times.

Figure 8 illustrates how the prediction error changes in practice as K varies. Here, we use CT-OT Flow with the ODE/SDE estimation setting, keeping all other parameters as in §5.2. As shown in Fig. 8, with appropriate values of K , CT-OT Flow achieves high-accuracy estimation of the dynamics. The dynamics prediction performance degrades significantly when K is too small, particularly around $K \approx 1$. This highlights the importance of Step 1 in the CT-OT Flow.

C Effect of the kernel smoothing parameter γ

We investigate how varying the kernel smoothing parameter γ affects the estimation results of CT-OT Flow. When γ is small, the estimated distribution $p_t(\mathbf{x})$ has nonzero density only around data points whose high-resolution time label is close to t . Conversely, when a large γ is used, the estimated density spreads more broadly, incorporating density contributions from data points with high-resolution time labels farther from t . Fig. 9 illustrates $\tilde{p}_t(\mathbf{x})$ at $t = 0.5$ for different values of γ .

Figure 10 illustrates how the prediction error changes in practice as γ varies. We run CT-OT Flow (ODE/SDE) with all other parameters as in §5.2, varying only γ . As shown in Figure 10, large γ values increase prediction errors. This is due to excessive smoothing, which diminishes the contribution of the estimated high-resolution time labels. On the other hand, using a very small γ results in increased errors for the Y-shaped and Arch datasets. As illustrated in Fig. 7, the accuracy of high-resolution time label estimation is lower for the Y-shaped and Arch datasets compared to Spiral. When γ is too small, the dynamics estimation becomes more sensitive to errors in the inferred high-resolution time labels, which likely leads to the observed degradation in overall performance. These results demonstrate that Step 2’s smoothing mitigates time-label errors and enhances overall estimation accuracy. We present the ablation study for Step 2 in App. K.3.

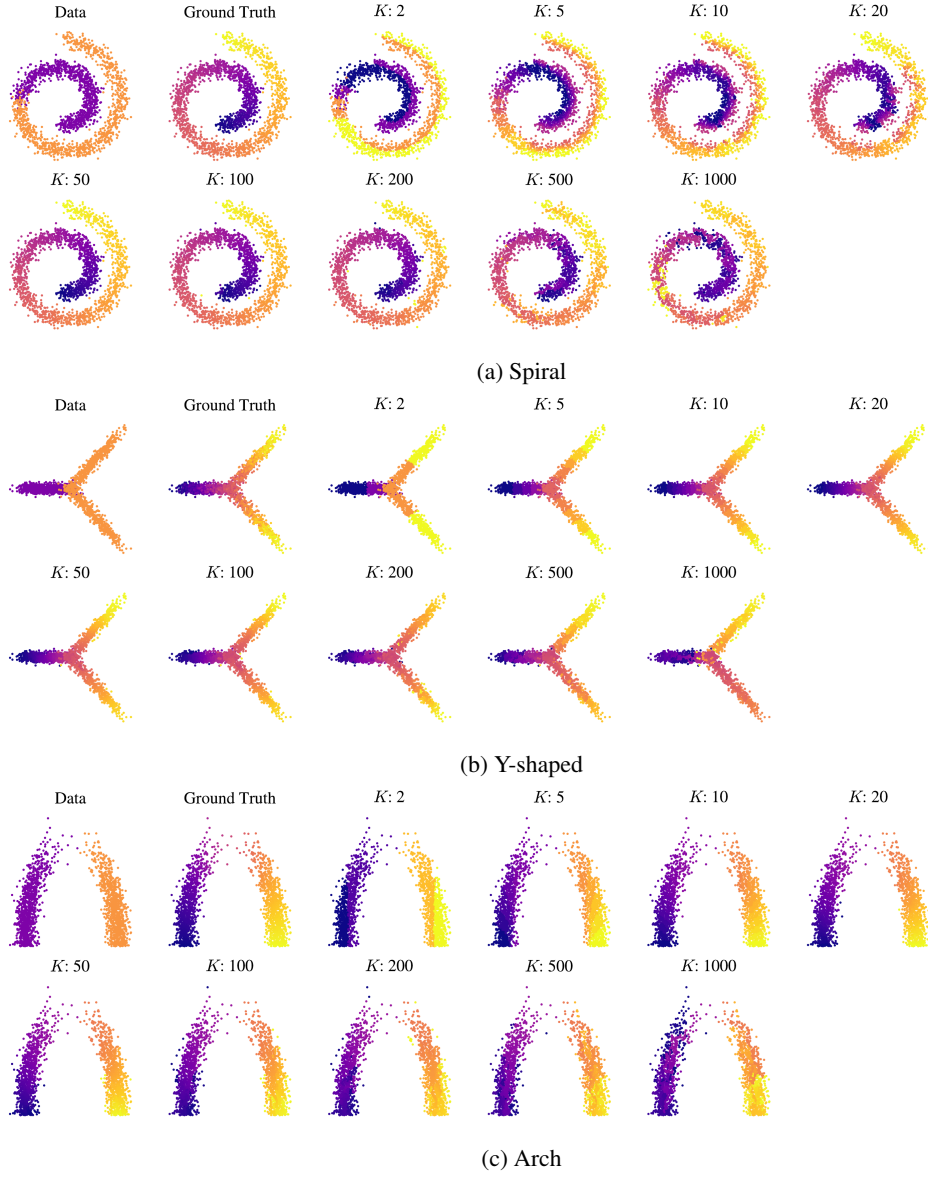


Figure 6: Estimated high-resolution time labels with varying K .

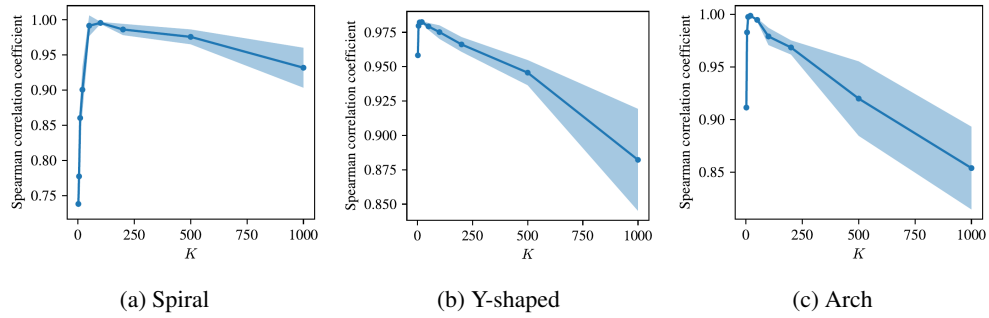


Figure 7: Spearman correlation between estimated high-resolution time labels and true times with varying K . The lines and areas represent the average and standard deviations, respectively.

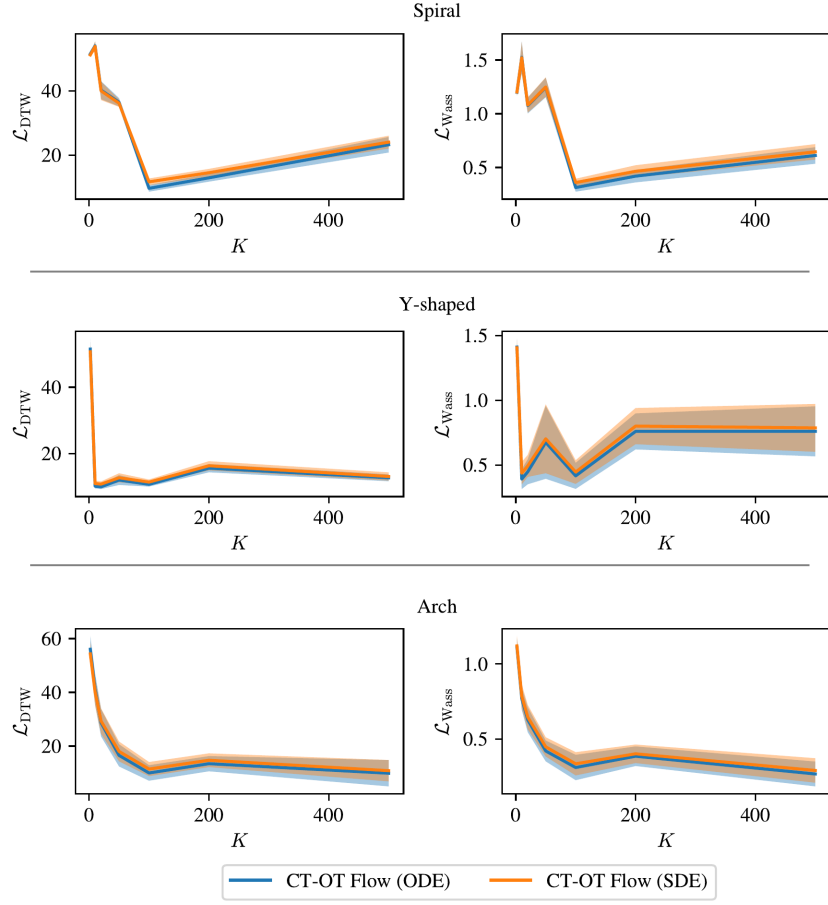


Figure 8: Prediction errors with varying K .

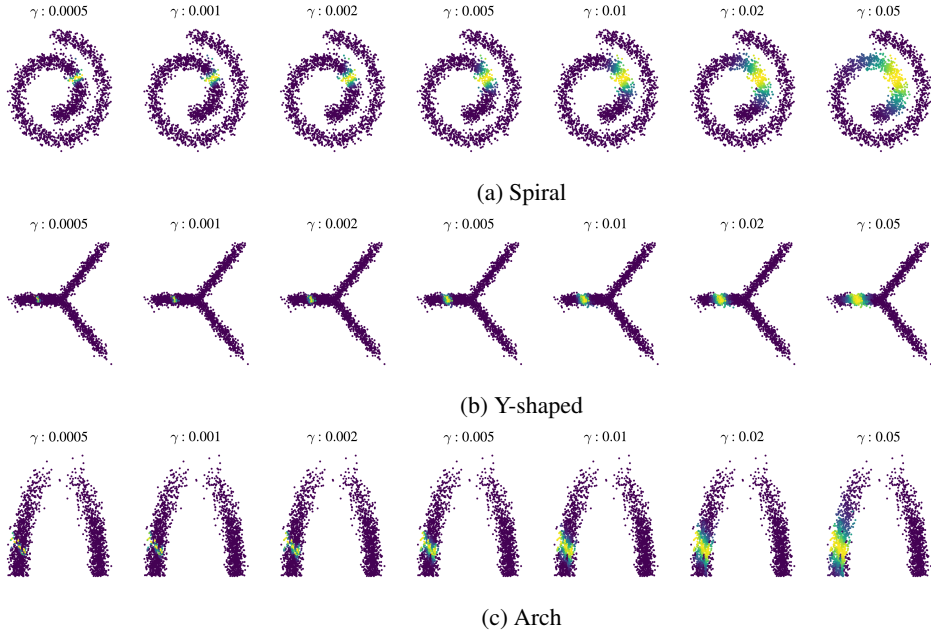


Figure 9: Estimated $\tilde{p}_t(\mathbf{x})$, where $t = 0.5$ with varying γ .

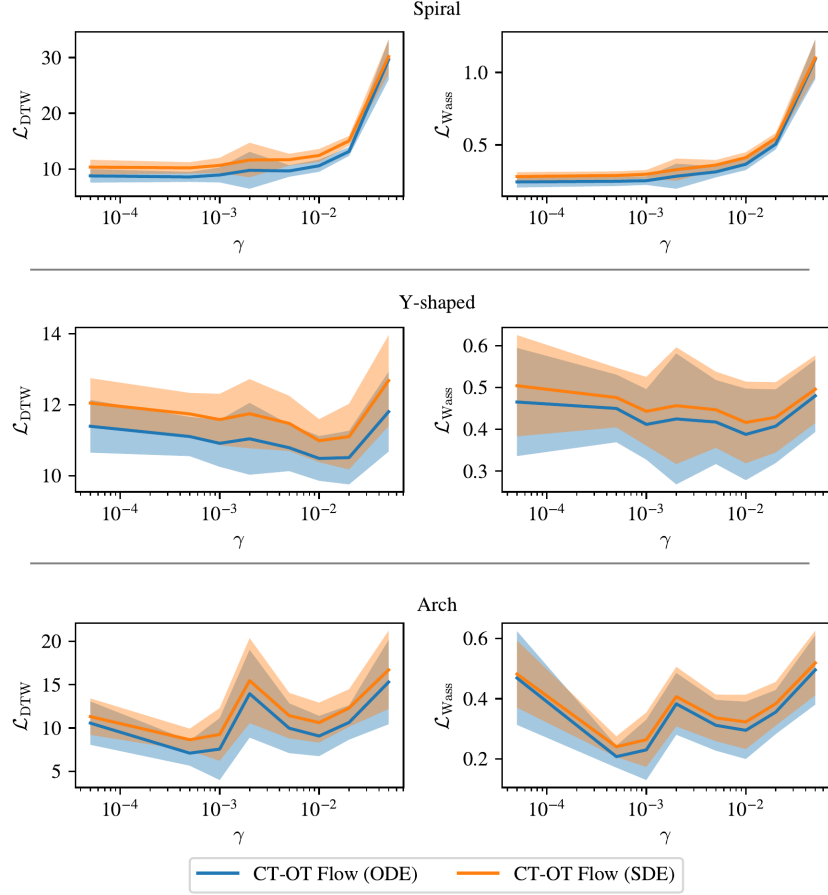


Figure 10: Prediction errors with varying γ .

D Assumption of Non-uniform $p(t)$

In the main text, we assumed $p(t)$ to be uniform within each interval due to lack of prior knowledge. In reality, however, $p(t)$ can be non-uniform. Retaining the uniform assumption when $p(t)$ is non-uniform causes the estimated velocity magnitude to deviate from the true value.

To illustrate this point, consider the simplest one-dimensional example $x(t) = t$, which has constant velocity $dx/dt = 1$. Suppose instead that $p(t)$ on $t \in [0, 2]$ has the triangular form

$$p(t) \propto \begin{cases} -a(t-1) + b & \text{if } t < 1, \\ a(t-1) + b & \text{otherwise,} \end{cases} \quad (17)$$

with $b > 0$. When $a = 0$, $p(t)$ reduces to the uniform case; when $a \neq 0$, the distribution becomes non-uniform and the data density varies over time.

Figure 11 compares histograms of data sampled from a uniform distribution ($a = 0, b = 1$) and a non-uniform distribution ($a = 5, b = 1$) (shown in the top panels). The bottom panels depict the velocities inferred by CT-OT Flow when the input consists of two time intervals, $X_{[0,1]}$ and $X_{[1,2]}$. Under the uniform $p(t)$, the estimated velocity remains close to 1, which is consistent with the true velocity. In contrast, when $p(t)$ is non-uniform, the estimated velocity tends to be lower in regions of higher data density (i.e., where $p(t)$ is larger) and higher in regions of lower density. This observation reflects a fundamental difficulty, without prior knowledge of $p(t)$, one cannot distinguish whether the observed variability is due to a non-uniform distribution $p(t)$ or an inherently time-varying velocity.

When prior knowledge about $p(t)$ is available, CT-OT Flow incorporates it via Eqs. (11)–(12). Figure 12 compares, for $a = 5, b = 1$, (left) high-resolution time labels and (right) velocities under

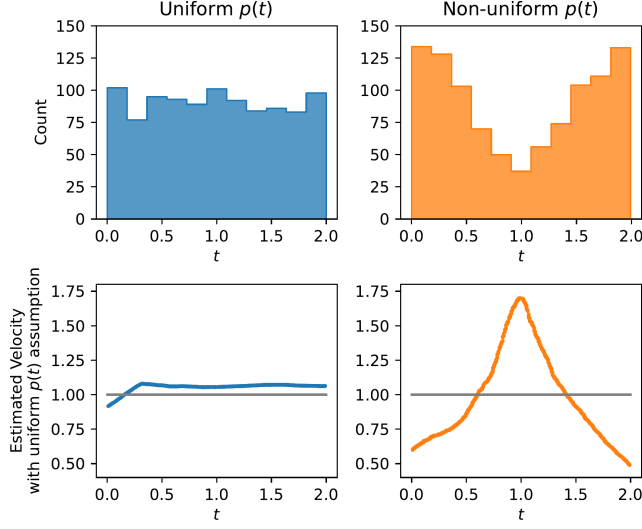


Figure 11: Estimated velocity (top) and sample histograms (bottom) if $p(t)$ is uniform (left) versus non-uniform (right).

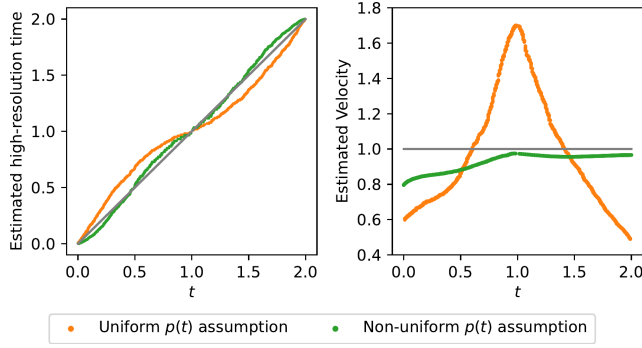


Figure 12: Estimated high-resolution time labels (left) and estimated velocities (right).

uniform versus non-uniform $p(t)$ assumptions. As shown, by incorporating the prior knowledge of $p(t)$, the accuracy of the estimated high-resolution time labels and the corresponding velocities can be improved. However, in real-world scenarios, it is often difficult to obtain the inverse CDF of $p(t)$. Note that the uniform $p(t)$ assumption remains a pragmatic choice when no prior information is available.

E Continuous relaxation of the mixed-integer linear program

E.1 Proof of Proposition 1

Here, we prove Proposition 1 stated in §4.3.

Proposition 1. *The problem in Eq. (8) is the continuous relaxation of the MILP in Eq. (7).*

Proof. The MILP (7) selects subsets S^- and S^+ from $X_{[t_{j-1}, t_j]}$ and $X_{[t_j, t_{j+1}]}$, respectively, to minimize the 2-Wasserstein distance between the corresponding empirical distributions. For simplicity, let us denote $X^- = X_{[t_{j-1}, t_j]}$ and $X^+ = X_{[t_j, t_{j+1}]}$ with $N^- = |X^-|$ and $N^+ = |X^+|$. Let $\mathbf{x}_-^{(i)}$ be the i -th point in X^- and $\mathbf{x}_+^{(j)}$ be the j -th point in X^+ . Define indicator vectors $\mathbf{z}^- \in \{0, 1\}^{N^-}$ and

$\mathbf{z}^+ \in \{0, 1\}^{N^+}$ such that:

$$z_i^- = \begin{cases} 1 & \text{if } \mathbf{x}_-^{(i)} \in S^- \\ 0 & \text{otherwise} \end{cases}, \quad z_j^+ = \begin{cases} 1 & \text{if } \mathbf{x}_+^{(j)} \in S^+ \\ 0 & \text{otherwise} \end{cases}. \quad (18)$$

The MILP in Eq. (7) can be written as:

$$\min_{\mathbf{z}^-, \mathbf{z}^+} \min_{P' \in U'_{(\mathbf{z}^-, \mathbf{z}^+)}} \sum_{i=1}^{N^-} \sum_{j=1}^{N^+} P'_{ij} \|\mathbf{x}_-^{(i)} - \mathbf{x}_+^{(j)}\|_2^2, \quad \text{s.t.} \quad \sum_{i=1}^{N^-} z_i^- = N_z^-, \quad \sum_{j=1}^{N^+} z_j^+ = N_z^+, \quad (19)$$

where N_z^- and N_z^+ are the number of the selected points that correspond to $|S^-| = \left\lceil \frac{|X_{[t_{j-1}, t_j]}|}{K} \right\rceil$ and $|S^+| = \left\lceil \frac{|X_{[t_j, t_{j+1}]}|}{K} \right\rceil$, respectively. The feasible set $U'_{(\mathbf{z}^-, \mathbf{z}^+)}$ is

$$U'_{(\mathbf{z}^-, \mathbf{z}^+)} = \left\{ P' \in [0, 1]^{N^- \times N^+} \mid P' \mathbf{1}_{N^+} = \frac{1}{N_z^-} \mathbf{z}^-, (P')^\top \mathbf{1}_{N^-} = \frac{1}{N_z^+} \mathbf{z}^+, \mathbf{1}_{N^-}^\top P' \mathbf{1}_{N^+} = 1 \right\}. \quad (20)$$

Note that the row/column-sum constraints in Eq. (20) force $\sum_j P'_{ij} = 0$ whenever $z_i^- = 0$ and $\sum_i P'_{ij} = 0$ whenever $z_j^+ = 0$. Consequently $P'_{ij} = 0$ if $\mathbf{x}_-^{(i)} \notin S^-$ or $\mathbf{x}_+^{(j)} \notin S^+$; the summations in Eq. (19) therefore effectively range only over pairs $(\mathbf{x}_-^{(i)}, \mathbf{x}_+^{(j)}) \in S^- \times S^+$.

Next, we replace the indicator vectors \mathbf{z}^- and \mathbf{z}^+ with continuous variables $\tilde{\mathbf{z}}^- \in [0, 1]^{N^-}$ and $\tilde{\mathbf{z}}^+ \in [0, 1]^{N^+}$, relaxing the binary choice (selected/not selected) to a fractional choice (selected at some proportion). Accordingly, the feasible set $U'_{(\tilde{\mathbf{z}}^-, \tilde{\mathbf{z}}^+)}$ is

$$U'_{(\tilde{\mathbf{z}}^-, \tilde{\mathbf{z}}^+)} = \left\{ P' \in [0, 1]^{N^- \times N^+} \mid P' \mathbf{1}_{N^+} = \frac{1}{N_z^-} \tilde{\mathbf{z}}^-, (P')^\top \mathbf{1}_{N^-} = \frac{1}{N_z^+} \tilde{\mathbf{z}}^+, \mathbf{1}_{N^-}^\top P' \mathbf{1}_{N^+} = 1 \right\}, \quad (21)$$

and $\sum_{i=1}^{N^-} \tilde{z}_i^- = N_z^-$, $\sum_{j=1}^{N^+} \tilde{z}_j^+ = N_z^+$. These constraints can be transformed into a manner equivalent to partial transport conditions:

$$\left(\sum_{i=1}^{N^-} z_i^- = N_z^- \right) \wedge \left(P' \mathbf{1}_{N^+} = \frac{1}{N_z^-} \tilde{\mathbf{z}}^- \right) \wedge (\mathbf{1}_{N^-}^\top P' \mathbf{1}_{N^+} = 1) \quad (22)$$

$$\Rightarrow \left(P' \mathbf{1}_{N^+} \leq \frac{1}{N_z^-} \mathbf{1}_{N^-} \right) \wedge (\mathbf{1}_{N^-}^\top P' \mathbf{1}_{N^+} = 1) \\ \left(\sum_{j=1}^{N^+} z_j^+ = N_z^+ \right) \wedge \left((P')^\top \mathbf{1}_{N^-} = \frac{1}{N_z^+} \tilde{\mathbf{z}}^+ \right) \wedge (\mathbf{1}_{N^-}^\top P' \mathbf{1}_{N^+} = 1) \quad (23)$$

$$\Rightarrow \left((P')^\top \mathbf{1}_{N^-} \leq \frac{1}{N_z^+} \mathbf{1}_{N^+} \right) \wedge (\mathbf{1}_{N^-}^\top P' \mathbf{1}_{N^+} = 1)$$

Obviously, $\tilde{\mathbf{z}}^-$ (and $\tilde{\mathbf{z}}^+$) that satisfies the left condition exists if the right condition holds. Hence, the original problem (Eq. (19)) transforms into

$$\min_{P \in U_{(\frac{N_z^-}{N_z^-}, \frac{N_z^+}{N_z^+})}} \sum_{i=1}^{N^-} \sum_{j=1}^{N^+} P_{ij} \|\mathbf{x}_-^{(i)} - \mathbf{x}_+^{(j)}\|_2^2, \quad (24)$$

where

$$U_{(\frac{N_z^-}{N_z^-}, \frac{N_z^+}{N_z^+})} = \left\{ P \in [0, 1]^{N^- \times N^+} \mid P \mathbf{1}_{N^+} \leq \frac{1}{N_z^-} \mathbf{1}_{N^-}, P^\top \mathbf{1}_{N^-} \leq \frac{1}{N_z^+} \mathbf{1}_{N^+}, \mathbf{1}_{N^-}^\top P \mathbf{1}_{N^+} = 1 \right\}. \quad (25)$$

Thus, the POT formulation in Eq. (24) shares exactly the same objective function as the original MILP in Eq. (19), while its feasible set contains the discrete feasible set obtained when the indicator variables are restricted to $\{0, 1\}$. Hence Eq. (24) is a continuous relaxation of Eq. (19): every integer-feasible solution is feasible for the relaxed POT problem. \square

E.2 Continuous relaxation for $k \geq 2$

we now provide a proof of the following proposition concerning the continuous relaxation of the optimization problem in Eqs. (9) and (10) in §4.3.

Proposition 2. *For $k = 1, \dots, K - 2$, the two optimization problems below become $POT_{(1, K-k)}(\hat{p}_{S_k^-}, \hat{p}_{X_{[t_{j-1}, t_j]} \setminus \cup_{k'=1}^k S_{k'}^-})$ and $POT_{(1, K-k)}(\hat{p}_{S_k^+}, \hat{p}_{X_{[t_j, t_{j+1}]} \setminus \cup_{k'=1}^k S_{k'}^+})$, respectively, when relaxed to continuous variables:*

$$\min_{S_{k+1}^- \subset X_{[t_{j-1}, t_j]} \setminus \cup_{k'=1}^k S_{k'}^-} \mathcal{W}^2(\hat{p}_{S_k^-}(\mathbf{x}), \hat{p}_{S_{k+1}^-}(\mathbf{x})) \quad (\text{backward}) \quad (9)$$

$$\min_{S_{k+1}^+ \subset X_{[t_j, t_{j+1}]} \setminus \cup_{k'=1}^k S_{k'}^+} \mathcal{W}^2(\hat{p}_{S_k^+}(\mathbf{x}), \hat{p}_{S_{k+1}^+}(\mathbf{x})) \quad (\text{forward}) \quad (10)$$

Proof. Consider first the optimization problem Eq. (9). Let $\mathbf{x}_-^{(i)} \in X_{[t_{j-1}, t_j]} \setminus \cup_{k'=1}^k S_{k'}^-$ and $\mathbf{x}_+^{(j)} \in S_k^-$. As in App. E.1, define an indicator vector \mathbf{z}^- by

$$z_i^- = \begin{cases} 1 & \text{if } \mathbf{x}_-^{(i)} \in S_{k+1}^-, \\ 0 & \text{otherwise.} \end{cases} \quad (26)$$

Then this MILP can be written as

$$\min_{\mathbf{z}^-} \min_{P'' \in U''_{(\mathbf{z}^-, 1)}} \sum_{i=1}^{N_k^-} \sum_{j=1}^{N_k^+} P''_{ij} \|\mathbf{x}_-^{(i)} - \mathbf{x}_+^{(j)}\|_2^2, \quad \text{s.t.} \quad \sum_{i=1}^{N_k^-} z_i^- = N_z^-, \quad (27)$$

where $N_k^- = |X_{[t_{j-1}, t_j]} \setminus \cup_{k'=1}^k S_{k'}^-|$, $N_k^+ = |S_k^-|$, and

$$U''_{(\mathbf{z}^-, 1)} = \left\{ P'' \in [0, 1]^{N^- \times N^+} \mid P'' \mathbf{1}_{N^+} = \frac{1}{N_z^-} \mathbf{z}^-, (P'')^\top \mathbf{1}_{N^-} = \frac{1}{N^+} \mathbf{1}_{N^+}, \mathbf{1}_{N^-}^\top P'' \mathbf{1}_{N^+} = 1 \right\}. \quad (28)$$

Note that, unlike in the previous MILP, all data in S_k^- are transported, i.e., $(P'')^\top \mathbf{1}_{N^-} = \frac{1}{N^+} \mathbf{1}_{N^+}$. By relaxing \mathbf{z}^- to continuous values, we obtain:

$$U_{(\frac{N_z^-}{N^+}, 1)} = \left\{ P \in [0, 1]^{N^- \times N^+} \mid P \mathbf{1}_{N^+} \leq \frac{1}{N_z^-} \mathbf{1}_{N^-}, P^\top \mathbf{1}_{N^-} = \frac{1}{N^+} \mathbf{1}_{N^+}, \mathbf{1}_{N^-}^\top P \mathbf{1}_{N^+} = 1 \right\}. \quad (29)$$

Setting $\frac{N_z^-}{N^+} = K - k$ yield the POT problem

$$POT_{(K-k, 1)}(\hat{p}_{X_{[t_{j-1}, t_j]} \setminus \cup_{k'=1}^k S_{k'}^-}, \hat{p}_{S_k^-}) \quad (30)$$

A similar argument holds for Eq. (10) (the forward case). Hence, by continuous relaxation, each step's MILP can be interpreted as a POT problem. \square

F Algorithm for CT-OT Flow

Algorithm 1 outlines the procedure for CT-OT Flow.

Algorithm 1 Dynamics estimation using CT-OT Flow

```
1: Input: Datasets  $\{X_{[t_j, t_{j+1}]}\}_{j=1}^T$ 
2: Output: Continuous-time distribution  $\tilde{p}_t(x)$  and ODE/SDE model
   Step 1: high-resolution time label estimation
3: for  $j = 1, \dots, T - 1$  do
4:   extract subsets  $S^-$  and  $S^+$  via Eq. (8)
5:   for  $k = 1$  to  $K - 2$  do
6:     extract subsets  $S_{k+1}^\pm$  via forward/backward selection via Eqs.(9) and (10).
7:   end for
8:    $S_K^- = X_{[t_{j-1}, t_j]} \setminus \cup_{k=1}^{K-1} S_k^-$ 
9:    $S_K^+ = X_{[t_j, t_{j+1}]} \setminus \cup_{k=1}^{K-1} S_k^+$ 
10: end for
11: assign each data point  $x^{(i)}$  a high-resolution time label  $\tilde{t}^{(i)}$  via Eqs. (11) and (12).
   Step 2: kernel-based time-smoothing of data distributions
12: Construct  $\tilde{p}_t(x)$  via Eq. (13).
   Step 3: ODE/SDE training
13: for  $n = 1$  to  $N_{\text{iter}}$  do
14:   draw sample pairs  $(x^{(0)}, x^{(1)})$  from  $\tilde{p}_t(x)$  and  $\tilde{p}_{t+\delta t}(x)$ 
15:   Update model parameters under an ODE/SDE training loss (e.g., Eq. (14)).
16: end for
17: return  $\tilde{p}_t(x)$  and the trained ODE/SDE model
```

G Computation time

The runtime of CT-OT Flow depends on the number of data points per interval N and the subdivision factor K . We present two acceleration techniques: screening and mini-batching. We then investigate how the actual computation time changes as N and K vary using network simplex algorithm [35] with the techniques and Sinkhorn iterations [29].

G.1 Fast computation via screening

Screening reduces cost by pre-filtering irrelevant points before POT. Although POT is applied over all points to capture boundary regions between contiguous intervals, only points near those boundaries meaningfully contribute to the transport plan. Points that are far from all points in the opposite group are unlikely to be selected as transport pairs and are therefore redundant in the optimization.

Screening removes such irrelevant points prior to POT optimization, using only the pairwise distance matrix. Let D denote the pairwise distance matrix between two point sets, $\mathbf{x}^{(m)} \in X$ and $\mathbf{y}^{(n)} \in Y$. The following points are excluded during the screening process:

$$\{\mathbf{x}^{(m)} \in X \mid \min_n D_{mn} > \alpha\}, \quad \{\mathbf{y}^{(n)} \in Y \mid \min_m D_{mn} > \beta\}, \quad (31)$$

where α and β are distance thresholds.

This pre-filtering step significantly reduces the number of candidate points and accelerates computation. The thresholds α and β can be adjusted so that, for example, $c \frac{N}{K}$ data points (i.e., c times the number of selected points) are retained from each interval for the POT computation. If c is sufficiently large, the solution to the POT problem remains almost unchanged, and the high-resolution time labels obtained by CT-OT Flow are also unaffected.

Figure 13 illustrates Spearman’s rank correlation between the estimated high-resolution time labels and the ground truth with varying the screening parameter c over 5 runs. As shown in Fig. 13, setting $c = 10$ already yields the high Spearman’s rank correlation of over 0.99.

G.2 Fast computation with mini-batches

Mini-batching reduces cost by partitioning each interval’s data into disjoint batches of size m . When the total number of points per interval N is very large, applying CT-OT Flow to the entire set becomes

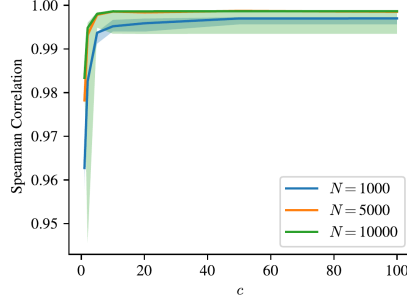


Figure 13: Spearman correlation between the estimated high-resolution time labels with screening setting ($c > 0$) and ground truth.

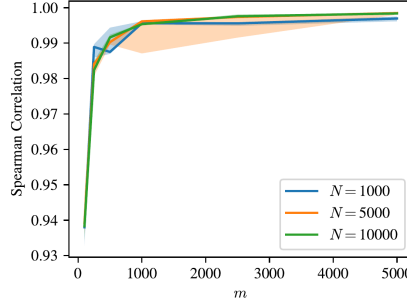


Figure 14: Spearman correlation between the high-resolution time labels with mini-batch setting and ground truth. The areas corresponds 0.25 and 0.75 quantiles.

prohibitively expensive; as shown in App. G.3, even with screening it is infeasible when $N > 10^6$. A simple remedy is to randomly split the dataset into $G = \lceil N/m \rceil$ mini-batches of size m and run Step 1 of CT-OT Flow independently on each. If the mini-batch size is sufficiently large, the induced error in the inferred high-resolution labels is expected to be negligible; the labels thus closely approximate those obtained by a full-data run. For fixed m , total cost scales linearly with N , enabling scalability to massive datasets. The mini-batch size m controls the trade-off between accuracy and runtime.

Figure 14 shows the Spearman’s rank correlation between the ground truth and high-resolution time labels from the mini-batch setting as m and N vary. Figure 14 shows that with $m = 1,000$, the Spearman’s rank correlation between the inferred high-resolution times from mini-batches and the ground truth exceeds 0.99.

G.3 Empirical runtime

We benchmarked Step 1 runtimes using the network simplex algorithm and the Sinkhorn solver [29] (entropic regularization $\epsilon = 0.1$). For Sinkhorn, we set a maximum of 10^4 iterations and a convergence tolerance of 10^{-9} . We also applied the screening method (with $c = 10$) and the mini-batch method (with $m = 1,000$) using the network simplex solver. Experiments with the simplex algorithm were run on a CPU (AMD EPYC 7742 64-core, single thread), while Sinkhorn iterations were executed on a GPU (NVIDIA A100 40 GB).

Figure 15 shows runtimes for (i) $K = 100$ with varying N , and (ii) $N = 5,000$ with varying K . Runtimes increase monotonically with N for all methods. For $N > 10,000$, Sinkhorn outperforms simplex, although it cannot run beyond $N \approx 30,000$ due to GPU memory limits. Even for $N = 100,000$, screening ($c = 10$) recovers high-resolution labels in tens of minutes on CPU only, while mini-batching yields labels in approximately 30 s. The effect of K on runtime is minor, but smaller K (i.e., matching more points per iteration) slows convergence. For a typical setting ($K \approx 100$), screening and mini-batch methods exhibit faster runtime than the network simplex algorithm. Additionally, for $N = 1,000,000$, our mini-batch setting ($m = 1,000$) achieves a

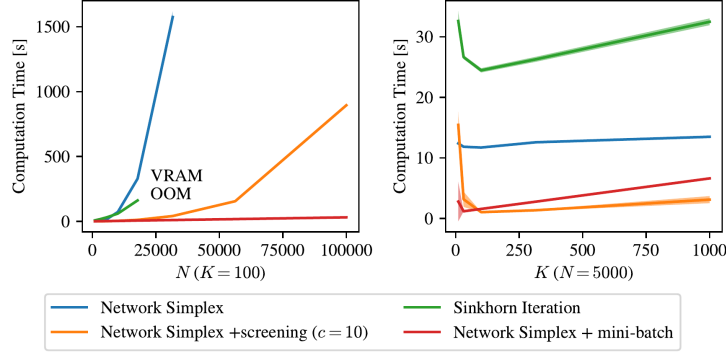


Figure 15: Runtimes of Step 1. Lines indicate means and shaded areas the 25th–75th quantiles over 5 runs. “OOM” marks out-of-memory failures.

Spearman’s rank correlation of 0.994 between the high-resolution time labels and the ground truth with a runtime of approximately 480 s on a single CPU.

H Parameters

Table 3 summarizes the hyperparameters used in our experiments. For OT-CFM [10], $[SF]^2M$ [2], MFM [26], and ENOT [20], the parameters were set according to the publicly available implementation at <https://github.com/atong01/conditional-flow-matching> (accessed on February 18, 2025), <https://github.com/KrishnaswamyLab/TrajectoryNet> (accessed on February 18, 2025), <https://github.com/kksniak/metric-flow-matching> (accessed on March 5, 2025), and <https://github.com/ngushchin/EntropicNeuralOptimalTransport> (accessed on April 12, 2025) respectively. We follow prior work in using the Euclidean distance as the ground metric for computing the 1-Wasserstein distance.

I Handling non-contiguous time intervals

Although CT-OT Flow assumes contiguous intervals, it can be applied to non-contiguous intervals as in the Arch dataset (§5.2). Accuracy on non-contiguous data depends on whether the CT-OT Flow assumption, (i.e., subsets with similar true times have smaller Wasserstein distance), remains valid.

Figure 16 shows the estimated high-resolution time labels after removing the middle time-interval data from each synthetic dataset in §5.2. In the figure, gray points indicate excluded samples, while the color of each remaining point represents its estimated high-resolution time label. As the figure shows, excluding these data points alters the results for the Spiral dataset, whereas it does not affect the Y-shaped and Arch datasets significantly. In the Spiral dataset with non-contiguous intervals, the central and outer subsets are close in Wasserstein distance despite being far apart in time. As a result, this assumption is violated, and the estimated high-resolution time labels deviate from the ground truth. By contrast, for the Y-shaped and Arch datasets, the assumption holds even with non-contiguous intervals, enabling accurate high-resolution time label estimation.

J Datasets

J.1 Synthetic datasets

We evaluate the ODE/SDE methods on the following three synthetic datasets:

1. Spiral: At each time t , the data distribution $p_t^*(\mathbf{x})$ is defined as a Gaussian with covariance σI , where I is the identity matrix and $\sigma = 0.1$. The trajectory X_j^* consists of the means of these Gaussians. The time intervals are $[0, 1]$ and $[1, 2]$.

Table 3: List of default parameters.

Model	Hyperparameters	Values
CT-OT Flow	K	100 (unless otherwise stated)
	γ	0.005 (unless otherwise stated)
	δt	0.1
	POT solver	Python Optimal Transport [38]
	POT Computation Method	Network simplex [35]
I-/OT-CFM [10] [SF] ² M [2]	Gradient Norm Clipping	0.1
	Learning Rate	1e-4
	Number of Iterations	5000
	Batch Size	128
	Number of Hidden Layers	3 (Full Connected)
	Number of Hidden Nodes	64
	Activation Function	selu [39]
	σ	0.1
MFM [26]	Batch Size	128
	γ	0.125
	ρ	0.001
	n_center	100
	κ	1.0
	Metric Network Learning Rate	1e-2
	Metric Network Optimizer	Adam [40]
	Metric Network Number of Epochs	50
	Geopath Network Learning Rate	1e-4
	Geopath Network Optimizer	Adam [40]
	Geopath Network Weight Decay	1e-5
	Flow Network Learning Rate	1e-3
	Flow Network Optimizer	AdamW [41]
	Flow Network Weight Decay	1e-3
	Flow Network σ	0.1
ENOT [20]	Number of Iterations	1000
	Number of Inner Iterations	10
	ϵ	0.1
	Shift Model Number of Hidden Layers	3 (Full Connected)
	Shift Model Number of Hidden Nodes	100
	Shift Model Optimizer	Adam [40]
	Shift Model Learning Rate	0.0001
	Shift Model Number of Steps	100
	Beta Net Number of Hidden Layers	3 (Full Connected)
	Beta Net Number of Hidden Nodes	100
	Beta Net Optimizer	Adam [40]
	Beta Net Learning Rate	0.0001
TrajectoryNet [1]	Mode	Base
	Number of Iterations	10,000
	Number of Hidden Layers (Full Connected)	3
	Number of Hidden Nodes	64
	Activation Function	Tanh
	Batch Size	1000
	Optimizer	Adam
	Learning Rate	0.001
	Weight Decay	1e-5
	atol	1e-5
	rtol	1e-5

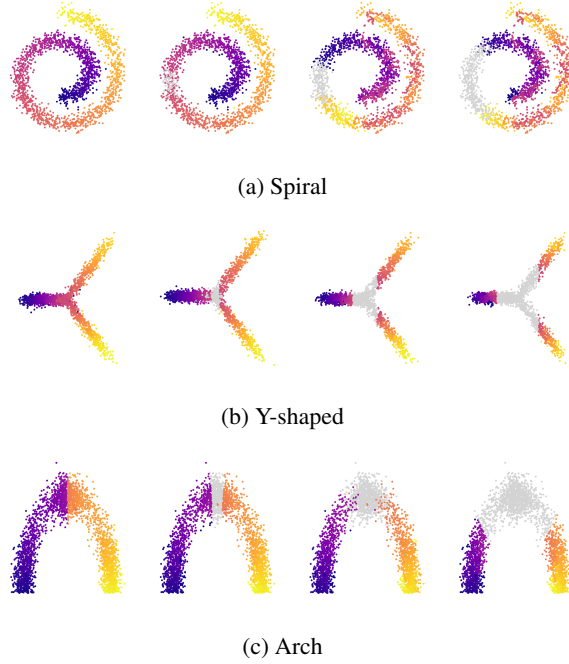


Figure 16: Estimated high-resolution time labels for non-contiguous time intervals.

2. Y-shaped: The distribution $p_t^*(\mathbf{x})$ is a mixture of two Gaussians. The trajectory X_j^* follows the paths traced by the means of these two components. The time intervals are $[0, 1]$ and $[1, 2]$.
3. Arch: We generate data following the procedure in [26]. The trajectory X_j^* is chosen as an arc passing through the center of the arch. The time intervals are $[0, 1]$ and $[2, 3]$.

The datasets are two-dimensional. In all datasets, we add i.i.d. Gaussian noise $\sim \mathcal{N}(0, 0.1)$ to each observation time. As a result, some data points near the boundary of a time interval may fall into a different interval than their true time. We set the number of samples per interval to 1000.

J.2 scRNA-seq datasets

We evaluated the ODE/SDE methods on two scRNA-seq datasets: Bifurcation and EB. The Bifurcation dataset [37, 33] consists of scRNA-seq measurements projected into four dimensional using principal component analysis (PCA). We grouped the first three labels (0 d, 1 d, 1.5 d) as $t = 0$, and then next three labels (2 d, 2.5 d, 3 d) as $t = 1$. The EB dataset [11] consists of preprocessed scRNA-seq measurements projected into two dimensions using the non-linear dimensionality reduction method PHATE [42]. We grouped the first two labels (Day 00-03, Day 06-09) as $t = 0$, and then next three labels (Day 12-15, Day 18-21, Day 24-27) as $t = 1$. For both datasets, we randomly split each timestamp’s data into 70% training and 30% testing sets, and evaluate models using the hold-out test data. These datasets are publicly available at <https://data.mendeley.com/datasets/v6n743h5ng/1> (Bifurcation; CC BY 4.0) and <https://github.com/yutongo/TIGON> (EB; MIT License).

K Additional results

K.1 Estimated trajectories

Figure 17 provides additional visualizations of the estimated trajectories for the Y-shaped, Arch, Bifurcation, and EB datasets. In each figure, the black lines indicate either the ground-truth or the estimated trajectories, depending on the method. For CT-OT Flow, the color of each point represents

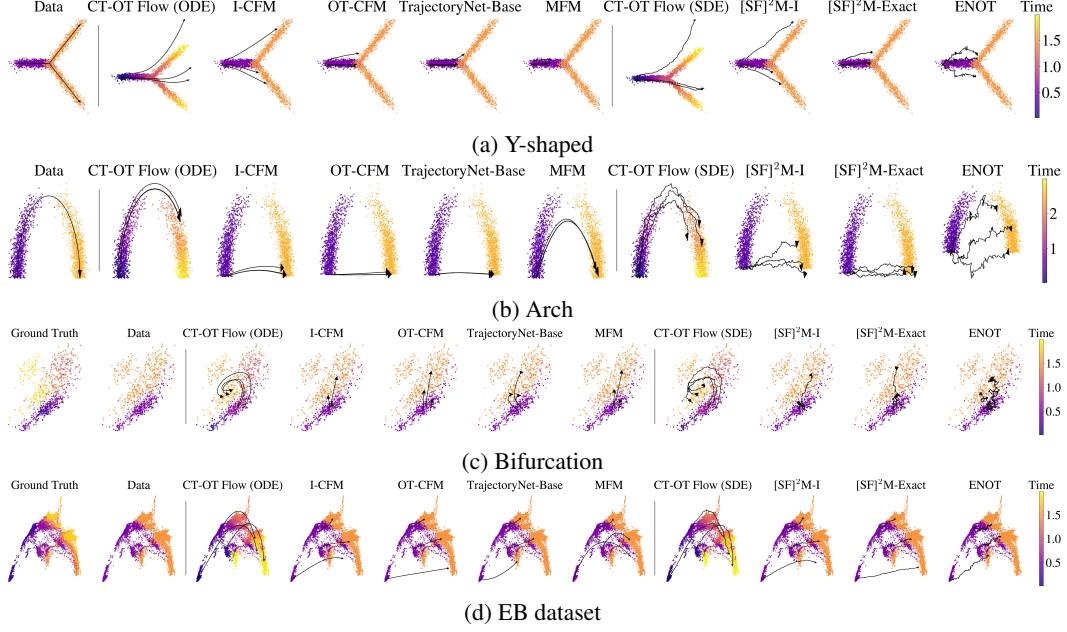


Figure 17: Estimated trajectories. The black lines indicate the true or estimated trajectories, while the color of each point in CT-OT Flow indicates its estimated high-resolution time label.

its estimated high-resolution time label, illustrating the model’s ability to resolve temporal ordering from coarse or noisy time labels. In Figs. 17(c) and (d), the leftmost figure illustrates the original timestamps, while the next figure illustrates the discretized timestamps.

In the Y-shaped and Arch datasets (Figs. 17(a) and (b)), CT-OT Flow successfully captures the geometry of the dynamics, even in the presence of temporal uncertainty. In the Bifurcation and EB datasets (Figs. 17(c) and (d)), which are constructed from scRNA-seq data, the model reconstructs plausible developmental trajectories and temporal progression from discretized temporal snapshots. These results demonstrate that CT-OT Flow can generalize to complex dynamics and real-world datasets, highlighting the robustness of the proposed method under various conditions.

K.2 Typhoon trajectory prediction

This section details the experiments using meteorological data in §5.4. We train a model using position data (longitude and latitude) sampled from typhoon tracks in Southeast Asia between 1951 and 2024. The raw data were obtained from <https://www.jma.go.jp/jma/jma-eng/jma-center/rsmc-hp-pub-eg/besttrack.html> (accessed on April 24, 2025) under the license compatible with CC BY 4.0; <https://www.jma.go.jp/jma/en/copyright.html>. The dataset records typhoon positions at 6-hour intervals from their onset.

From the full dataset, we extracted 528 trajectories that span at least 150 hours and constructed temporal snapshots by assigning $t = 0$ at 0 hours (onset), $t = 1$ at 72 hours, and $t = 2$ at 144 hours after onset. Note that the index in each temporal snapshot was randomized, and the models only had access to individual data points, not the trajectories. We split the trajectories into 70% for training and 30% for testing, and performed 10 evaluation runs with different neural network initializations. Before training, the longitude and latitude coordinates were normalized to have zero mean and unit variance. We used the Euclidean distance between points as the ground metric.

We evaluate each method by reconstructing trajectories in the test split, where the initial points are given at $t = 0$. We treat the empirical data distribution at each time t as the ground truth distribution $p_t^*(\mathbf{x})$ for computing $\mathcal{L}_{\text{Wass}}$, and the full trajectories themselves as X_j^* for \mathcal{L}_{DTW} . Table 4 summarizes the evaluation results. As shown in the table, CT-OT Flow significantly improves the accuracy of trajectory prediction. Note that CT-OT Flow (ODE) and CT-OT Flow (SDE) employ OT-CFM [10]

Table 4: Estimation errors (\mathcal{L}_{DTW} and $\mathcal{L}_{\text{Wass}}$) on the typhoon dataset. Bold: best within ODE/SDE groups; †: statistically significant vs. baselines ($p < 0.05$).

Method↓ Dataset→	\mathcal{L}_{DTW}	$\mathcal{L}_{\text{Wass}}$
CT-OT Flow (ODE)	16.59 $\pm 0.25^\dagger$	0.35 $\pm 0.05^\dagger$
OT-CFM [10]	17.16 ± 0.07	0.48 ± 0.01
CT-OT Flow (SDE)	16.48 $\pm 0.28^\dagger$	0.36 $\pm 0.05^\dagger$
[SF] ² M-Exact [2]	17.10 ± 0.07	0.49 ± 0.01

Table 5: Estimation errors (mean \pm std) for ablation study on the synthetic datasets. Bold: best within ODE/SDE groups; †: statistically significant vs. other settings ($p < 0.05$). w/o denotes “without”.

Dataset→	Spiral		Y-shaped		Arch	
Method↓ Metric→	\mathcal{L}_{DTW}	$\mathcal{L}_{\text{Wass}}$	\mathcal{L}_{DTW}	$\mathcal{L}_{\text{Wass}}$	\mathcal{L}_{DTW}	$\mathcal{L}_{\text{Wass}}$
CT-OT Flow (ODE)	9.64 $\pm 1.04^\dagger$	0.31 ± 0.04	10.79 $\pm 0.66^\dagger$	0.41 $\pm 0.10^\dagger$	9.98 ± 2.88	0.31 $\pm 0.08^\dagger$
w/o Step 2 (ODE)	12.72 ± 3.13	0.33 ± 0.07	16.26 ± 3.38	0.84 ± 0.27	9.86 ± 2.50	0.47 ± 0.14
w/o Step 1&2 (ODE)	51.41 ± 0.02	1.17 ± 0.00	29.41 ± 0.17	0.90 ± 0.00	31.68 ± 0.12	0.62 ± 0.00
CT-OT Flow (SDE)	11.66 ± 1.06	0.36 ± 0.04	11.47 $\pm 0.78^\dagger$	0.45 $\pm 0.09^\dagger$	11.43 ± 2.60	0.34 $\pm 0.08^\dagger$
w/o Step 2 (SDE)	13.27 ± 2.46	0.34 ± 0.05	16.92 ± 3.33	0.87 ± 0.28	10.04 ± 1.72	0.48 ± 0.14
w/o Step 1&2 (SDE)	51.33 ± 0.04	1.17 ± 0.01	28.99 ± 0.18	0.89 ± 0.00	31.01 ± 0.16	0.62 ± 0.00

and [SF]²M-Exact [2] for Step 3, respectively. These differences highlight the improvements in prediction accuracy resulting from the use of CT-OT Flow.

K.3 Ablation study: omitting steps in CT-OT Flow

We quantitatively evaluate how much each stage of CT-OT Flow contributes to the final accuracy. Recall that Step 1 assigns high-resolution time labels, while Step 2 converts them into continuous-time distributions $\hat{p}_t(\mathbf{x})$. In Step 3, we sample $t \sim \mathcal{U}(t_1, t_{T+1} - \delta t)$ and draw paired samples from \hat{p}_t and $\hat{p}_{t+\delta t}$ to train the ODE/SDE model.

We first completely omit Step 2. Instead of constructing continuous distributions, we directly use the high-resolution labels from Step 1. Specifically, we sample label values \tilde{t}_j from the set of unique high-resolution time labels, then form empirical distributions $\hat{p}_{\tilde{t}_j}(\mathbf{x})$ and $\hat{p}_{\tilde{t}_{j+1}}(\mathbf{x})$ using only points whose labels equal \tilde{t}_j and \tilde{t}_{j+1} , respectively. Table 5 compares the results from §5.2 against this ablated variant. We observe that omitting Step 2 degrades estimation accuracy, underscoring the importance of modeling continuous-time distributions in Step 2.

Next, we omit both Step 1 and Step 2, reverting to standard OT-CFM [10] or [SF]²M [2], which operate directly on the coarse snapshots. Performance drops even further (rows “w/o Step 1&2”), indicating that high-resolution time label estimation in Step 1 is beneficial, and that Step 2 provides an additional, complementary benefit.

K.4 CT-OT Flow for high-dimensional data

We evaluated CT-OT Flow by applying PHATE [42] to embed the EB dataset [11] into $d \in \{2, 4, 8, 16, 32\}$ dimensions. Table 6 summarizes the estimation errors $\mathcal{L}_{\text{Wass}}$ for each setting. Our experiments reveal that when using a small kernel smoothing parameter ($\gamma = 0.005$), CT-OT Flow’s performance degrades as the dimension increases. We attribute this to the concentration of pairwise distances in high-dimensional spaces, which reduces the contrast required for accurate boundary-point extraction. Conversely, increasing γ (e.g., $\gamma = 0.5$) yields robust $\mathcal{L}_{\text{Wass}}$ across all d . This is because a larger γ enhances the robustness of high-resolution time label estimation against the reduced distance contrast (see also App. C). In practice, when applying CT-OT Flow to high-dimensional data, one may either increase the kernel smoothing parameter γ or embed the data into a lower-dimensional space to effectively identify points near the interval boundaries.

Table 6: Estimation errors ($\mathcal{L}_{\text{Wass}}$) on the EB dataset with varying dimensions. Bold: best within ODE/SDE groups and dimension; †: statistically significant vs. other methods ($p < 0.05$).

Method↓ Dimension→	2	4	8	16	32
CT-OT Flow (ODE) ($\gamma = 0.005$)	0.94±0.11	1.13±0.06	2.19±0.13	6.41±0.88	5.80±0.46
CT-OT Flow (ODE) ($\gamma = 0.05$)	0.98±0.09	1.07 ±0.06†	1.76 ±0.08†	4.21±0.14	4.79±0.33
CT-OT Flow (ODE) ($\gamma = 0.5$)	0.81 ±0.05†	1.16±0.03	1.81±0.04	2.75 ±0.04	4.34±0.04
I-CFM [10]	1.00±0.01	1.32±0.01	2.01±0.01	2.86±0.01	4.36±0.01
OT-CFM [10]	1.06±0.01	1.37±0.01	2.01±0.01	2.87±0.01	4.32±0.01
TrajectoryNet [1]	1.10±0.04	2.04±0.59	3.07±0.16	4.16±0.29	5.41±0.27
MFM [26]	1.04±0.04	1.34±0.03	1.93±0.03	2.80±0.03	4.22 ±0.02†
CT-OT Flow (SDE) ($\gamma = 0.005$)	0.92±0.12	1.11±0.07	2.19±0.14	6.39±0.85	5.79±0.46
CT-OT Flow (SDE) ($\gamma = 0.05$)	0.97±0.09	1.04 ±0.06†	1.76 ±0.08†	4.25±0.16	4.79±0.32
CT-OT Flow (SDE) ($\gamma = 0.5$)	0.80 ±0.05†	1.14±0.03	1.79±0.04	2.72 ±0.04†	4.33±0.04
[SF] ² M-I [2]	0.99±0.01	1.30±0.01	2.00±0.01	2.84±0.01	4.34±0.01
[SF] ² M-Exact [2]	1.05±0.01	1.36±0.01	2.00±0.01	2.86±0.01	4.32 ±0.01
ENOT [20]	1.03±0.02	1.33±0.01	1.99±0.08	2.90±0.08	4.53±0.25

L Broader Impacts

CT-OT Flow enables applications in scientific domains including biology and medicine. By modeling continuous-time dynamics more accurately, CT-OT Flow could assist in understanding, e.g., cellular development. However, as with any statistical model, misuse or overinterpretation may yield misleading conclusions. Without prior knowledge, CT-OT Flow assumes uniform time distributions within intervals—an assumption that may not hold in all settings. Real-world applications should validate these assumptions and adopt safeguards accordingly.